
Article:
Zhang, Q., Lu, W., Scarpa, F. et al. (5 more authors) (2021) Topological characteristics and mechanical properties of uniaxially thermoformed auxetic foam. Materials and Design, 211. 110129. ISSN 0264-1275

https://doi.org/10.1016/j.matdes.2021.110139

Materials & Design 211 (2021) 110139

Contents lists available at ScienceDirect

Materials & Design

journal homepage: www.elsevier.com/locate/matdes

Topological characteristics and mechanical properties of uniaxially thermoformed auxetic foam

Qicheng Zhang [a], Wenjiang Lu [b], Fabrizio Scarpa [a,*], David Barton [c], Kathryn Rankin [d], Yunpeng Zhu [e], Zi-Qiang Lang [e], Hua-Xin Peng [b]

[a] Bristol Composites Institute, University of Bristol, BS8 1TR Bristol, UK
[b] Institute for Composites Science Innovation (InCSI), School of Materials Science and Engineering, Zhejiang University, Hangzhou 310027, PR China
[c] Department of Engineering Mathematics, University of Bristol, Merchant Venturers Building, BS8 1UB Bristol, UK
[d] μ-VIS X-ray Imaging Centre, University of Southampton, SO17 1BJ Southampton, UK
[e] Department of Automatic Control and Systems Engineering, University of Sheffield, Sheffield, UK

HIGHLIGHTS

- Auxetic foam produced via uniaxial thermoforming in thick blocks and variable volumetric compressions.
- Stiffness, Poisson's ratios and energy dissipated in quasi-static compression and tension tests.
- Topological and quantitative characterization of the foams via μ-CT scanning.
- High-fidelity and benchmarked Finite Element models of the foam microstructures.

GRAPHICAL ABSTRACT

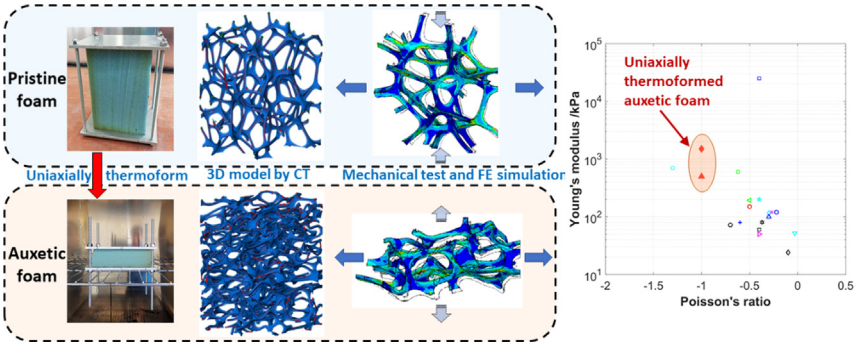

ARTICLE INFO

Article history:
Received 20 June 2021
Revised 15 September 2021
Accepted 29 September 2021
Available online 1 October 2021

Keywords:
Auxetic foam
Negative Poisson's ratio
Modulus
Loss factor
X-ray CT
Finite element method

ABSTRACT

We present here a simplified procedure to manufacture auxetic PU foam via a single direction thermoforming compression process applied to conventional (pristine) open cell foam samples. The auxetic foams produced here have a Poisson's ratio ν_{21} ranging from −1 to 0 in the 1–2 plane and a tangent modulus E_{t2} ranging from 0.2 MPa to 2 MPa. X-ray μ-CT and 3D skeletonization enabled the extraction of the topological parameters of the pristine and the auxetic foams. The auxetic foam is transverse isotropic with cell structures exhibiting a re-entrant shape along the thermoforming compression direction 1. More ribs are also oriented within the transverse plane 2–3, in which the stiffness is larger. Tensile and compression quasi-static tests have been carried out on samples cut along different directions and having various thermoforming compression ratios r_c. Auxeticity is present in the in 1–2 plane only for compression ratios between 40% and 80%. Finite Element models for the pristine and auxetic foams have also been built from the μ-CT scanned 3D models. The numerical results show a good agreement with the experimental data and help explaining the deformation mechanisms of these auxetic foams.

1. Introduction

Auxetic polyurethane (PU) foam is a type of porous metamaterial with negative Poisson's ratio [1,2]. Auxetic foams combine the advantages of the counter-intuitive auxetic deformation and the

* Corresponding author.
E-mail address: f.scarpa@bristol.ac.uk (F. Scarpa).

https://doi.org/10.1016/j.matdes.2021.110139
0264-1275/

use of PU foam material, thus leading to multifunctional properties such as indentation resistance [3], compliant shear [4–6], improved fracture resistance [7], synclastic behavior [8,9], high impact [10–14] and vibration [15] energy absorption, together with shape memory effect [16–21]. Auxetic foams have significant potential in applications ranging from personal protective equipment [22–25], noise reduction [26–28], cushioning [29], aircraft seats [30], filtration [31,32], smart materials and sensor applications [33–36].

However, auxetic PU foams have never been widely used in commercial applications partially due to their sophisticated and somehow complex manufacturing procedures. The manufacturing of auxetic PU foam was first developed by Lakes [37] and then modified by several other authors [24,38–42]. The classical manufacturing process to convert conventional PU foams into auxetic versions mainly includes a volumetric compression, annealing via heating, cooling and relaxation [11,42]. Volumetric compression is used to create the typical re-entrant cell structures of auxetic materials by buckling the foam ribs under high strain triaxial compression [39,42]. The heating and cooling are designed to thermoform the compressed foam by phase transition of the PU material at high temperature [17], so that the re-entrant cell structures could be stable after releasing the foam from the compressive state. Other methods to replace the heating and cooling steps have also been developed, notably by using compressed carbon dioxide [43] or solvents [44]. The triaxial volumetric compression process is usually carried out using special designed moulds involving lubrication by oil and manually compressing the foam [11,39,40,42,45], the latter in particular making mass production difficult. Some of the Authors here have used vacuum bags and autoclave systems to replace the rigid mould, but this approach has its own complexities [16,46]. Alderson et al. [47] have however manufactured thin auxetic foam sheets for sports applications by uniaxial thermoforming compression and multi-stage heating and annealing. The maximum reported thickness of those uniaxially thermoformed auxetic foam sheet is<4 mm. The auxetic foam sheet is designed to withstand compressive loading along the thermoform compression direction. The foam exhibits an auxetic behaviour under tension for samples with volumetric compression ratio between 40% and 60%.

In this work we show the effects of simplifying the triaxial volumetric compression commonly used in thermoforming by applying a uniaxial compression only and obtaining thick open cell foam blocks (>100 mm). Auxeticity only along the thermoforming compression direction can be observed in the transverse plane when under both compressive and tensile loads. Auxetic foams with different thermoforming compression ratio r_c have been manufactured and tested to study the effect of this uniaxial volumetric compression. This methodology has a considerable potential for the manufacture of large scale samples towards possible future routes to industrial production.

The mechanical properties of auxetic foam are mainly dictated by their internal microstructures [11]. In order to obtain the topological information pertinent to these foams, the most widely used method is observation by microscope, which can only provide images on surface layer of the foam sample [44,46–49]. X-ray micro computed tomography (μ-CT) scanning has also been used to obtain the internal structure of auxetic foams [33,50–57], but – to the best of our knowledge - the existing results are mostly with low spatial resolution (44 μm [52], 20 μm [50]) and some important topological information such as the distribution of the orientation of the ribs have not been extracted and compared in a quantitative manner. In this work we use high resolution (<1μm) μ-CT techniques to obtain the internal structure of our auxetic PU foam. Three-dimensional skeletonization algorithms have been successfully used by some researchers to analyze 3D models of fiber-filled porous materials, therefore extracting structural parameters such as the fiber orientation, fiber segment lengths and number of contact pairs [58–60]. Porous foam materials are mainly made of thin and long ribs and also suitable for the application of a 3D skeletonization algorithm [61–64], and we have adopted this specific approach in our work to identify ribs orientation maps for the pristine and auxetic foams previously applied by the Authors to porous metal systems made by networks of helix wires [58].

Theoretical models based on the structural configuration of auxetic open cell foams are built to help explain the deformation mechanisms and mechanical properties of those foams. Examples are the strut-level force model of Warren and Kraynik [65], the re-entrant unit cell model by Choi et al [66,67] and the semi-rigid rotating triangle model by Chetcuti et al [68]. Although these models help researchers to have a deeper understanding about the mechanical performance of auxetic foams, they are however highly simplified and often different from the real three-dimensional microstructures present inside the auxetic foams. On the contrary, Finite Element (FE) representations based on 3D solid models from CT scans can better reflect the deformation mechanisms inside manufactured auxetic foams. However, mechanical FE simulation works on auxetic foams and based on scans are quite rare in open literature. McDonald et al. [50] have performed FE simulations for conventional and auxetic foams under tension, but no compressive loading was included. Critchley et al. [1] only provided a schematic Finite Element model representation without further description or numerical results. In this work we present a series of FE models related to the mechanical properties of pristine and auxetic foams based on the μ-CT scanned 3D models, showing good agreement with the experimental results acquired under both tensile and compressive loading conditions. The fidelity of the FEA simulations presented here indicates that the baseline modelling could also be used in future analysis to understand the deformation mechanisms and the mechanical properties at multiple scales of foams and general porous materials.

2. Manufacturing process of the uniaxial thermoformed auxetic foam

The manufacturing procedure of the uniaxial thermoformed auxetic foam is illustrated in Fig. 1. The pristine open-cell polyurethane foam is supplied by the SM Upholstery Ltd. The foam has a density of 27.0 kg/m^3 and a pore linear density of 1102–1378/m. Seven pristine foam blocks with size of 120 × 120 × 160 mm are compressed along the height direction in an open mould down to 128 mm, 112 mm, 96 mm, 80 mm, 64 mm, 48 mm and 32 mm, corresponding to compression ratios r_c of 20%, 30%, 40%, 50%, 60%, 70% and 80% respectively (Fig. 1a). During compression, the pristine foam is compacted and then released to the needed size so that the deformation of the foam is more homogeneous throughout its height.

The compressed foam is then placed in an oven (Carbolite PF laboratory oven) together with the mould for thermoforming, with a thermocouple inserted at the center of the foam block to monitor the internal temperature. The profile of the ambient and inner temperatures is shown in Fig. 1b. The oven temperature is first increased to 145 °C at a rate of 5 °C/min, and then maintained constant. The temperature inside the foam increases slower than the ambient temperature due to the thermal insulation of the foam and tends to plateau when coming closer to the ambient temperature. The heating procedure is terminated 30 mins after the inner temperature reaches 135 °C, which is larger than the glass transition temperature of the foam (114 °C [17]). The foam and mould are then removed from the oven and cooled at room temperature

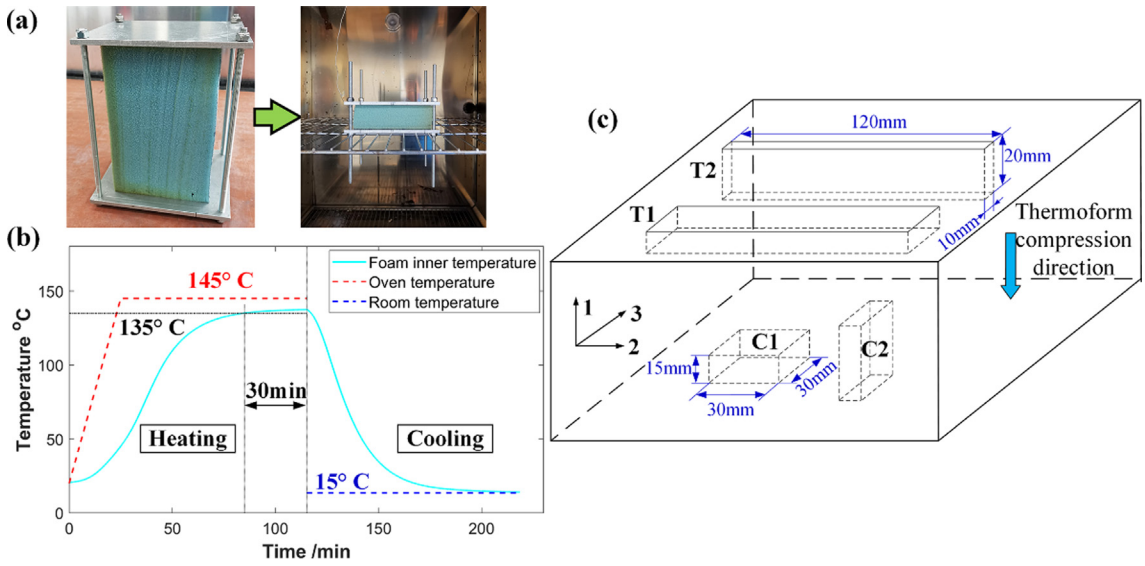

Fig. 1. Preparation of the auxetic foam specimens. Manufacturing procedure (a), temperature profile (b) and orientation of the specimens from the foam block (c).

(~15 °C). The total heating and cooling time of the different foam blocks with different r_c differ slightly because of the thermal insulation effect of foam blocks with different thickness. However, the time of 30 mins above 135 °C is always maintained the same. After the thermoforming procedure, auxetic re-entrant cell structures of the compressed foam appear to be stable and no evident thickness increase of the foam block is observed within a short time after removing the mould.

Two types of specimens (Type T and Type C) are cut from each auxetic foam block. These samples have different sizes and orientations, as well as different compression ratios r_c (Fig. 1c). Type T long rectangle specimens with size of 20 × 10 × 120 mm are used for tensile tests. Two T2 and one T1 specimens are cut as three parallel samples to compare and study the effect of the different width and depths along the thermoforming and transverse directions. Three C1 and three C2 specimens with size 30 × 30 × 15 mm are used for compressive test along the thermoforming compression direction 1 and the transverse direction 2, respectively.

3. Topological characteristics of the auxetic foam

Scanning electron microscopy images (Hitachi TM3030plus tabletop microscope) of the pristine and auxetic foams are shown in Fig. 2. Both the pristine and auxetic foams are reticulated with membranes present between some neighboring cells. There is an obvious difference between the structures of the auxetic foam observed along the compression direction 1 (Fig. 2 (b)-(h)) and the transverse direction 2 (Fig. 2 (j)-(p)); this indicates the presence of transverse isotropy due to the manufacturing process. The microstructures observed along d1 shows a partially original reticulated structure with kinks along the ribs. The overall configuration of the auxetic foam with different r_c values along d1 are quite similar, with more kinks and curved ribs appearing with increasing compression ratios. The microstructural configuration along d2 is however more elongated and compressed compared to the one along d1; the effect of r_c on the microstructures observed along the d2 direction is also much more significant. As the compression ratio increases, the ribs observed along d2 become more curved and twisted with higher tortuosity, and the overall porous configurations become denser.

μ-CT scanning was conducted on the pristine and auxetic foam with r_c = 30% and 60% using a Zeiss Xradia 160 kVp Versa 510 (Carl Zeiss Microscopy GmbH, Germany) at 80 kVp peak voltage and 6 W power, with a source-to-object distance of 16 mm and a source-to-detector distance of 54 mm. Using the 4× objective with 1× binning, a voxel resolution of 0.998 μm was achieved. 3201 projection images were acquired through 360 degrees rotation of the specimen with 2 s exposure time. The projection data was reconstructed using the Zeiss XM Reconstructor software (Carl Zeiss Microscopy GmbH, Germany) into TXM files, subsequently converted to 16 bit raw volumes.

The 3D model of the foam is processed and generated from CT data using the Avizo 2019 software. 3D Median filter was applied to reduce the noise of the data. The 3D model and three orthogonal sections of the auxetic foam with r_c = 60% are shown in Fig. 3. The scanned space of the specimen is in a cylinder shape with diameter of 1.938 mm and height of 1.979 mm. The curved ribs and partial membranes can be clearly observed in the 3D model. The cross sections of the ribs in the three sections have a triangle shape, in agreement with [55]. More cross sections of the ribs appear along the vertical sections B and C compared with the horizontal section A; this indicates that more ribs are oriented closer to 2–3 plane, as also observed in the SEM images (Fig. 2). Partial membranes with a thickness of ~3 μm are also clearly visible in the figures related to the three sections.

The 3D models of the pristine and auxetic foams with r_c = 30% and 60% are reconstructed from μ-CT are shown in Fig. 4 (a)-(c). Wrinkles can be observed on the edges of ribs where the membranes are connected. The mechanical properties of different foams are mainly determined by the configuration of ribs; the existence of thin membranes can contribute to the stiffness of the foam, but it will likely not play a dominant role. The membranes of the different foam specimens are removed from the images using algorithms including binary thresholding segment, erosion and dilation of 3 voxels in Avizo; this is done to simplify the 3D model for further observations, extraction of topological parameters and the finite element simulations. The processed 3D models of the three foams are shown in Fig. 4 (d)-(f), while the corresponding vertical sections cut by plane 1–3 are shown in Fig. 4 (g)-(i). The processed 3D model appears to describe well the overall structure of the original 3D model. In Fig. 4 (g)-(i), the black color in the section figures refers to original model while the blue one represents the processed model. The blue color covers the black area in all rib cross section regions and only ignores the thin membrane regions, showing a good coincidence between processed and original models. In the 3D models of pristine foam, the pores and cells are slightly

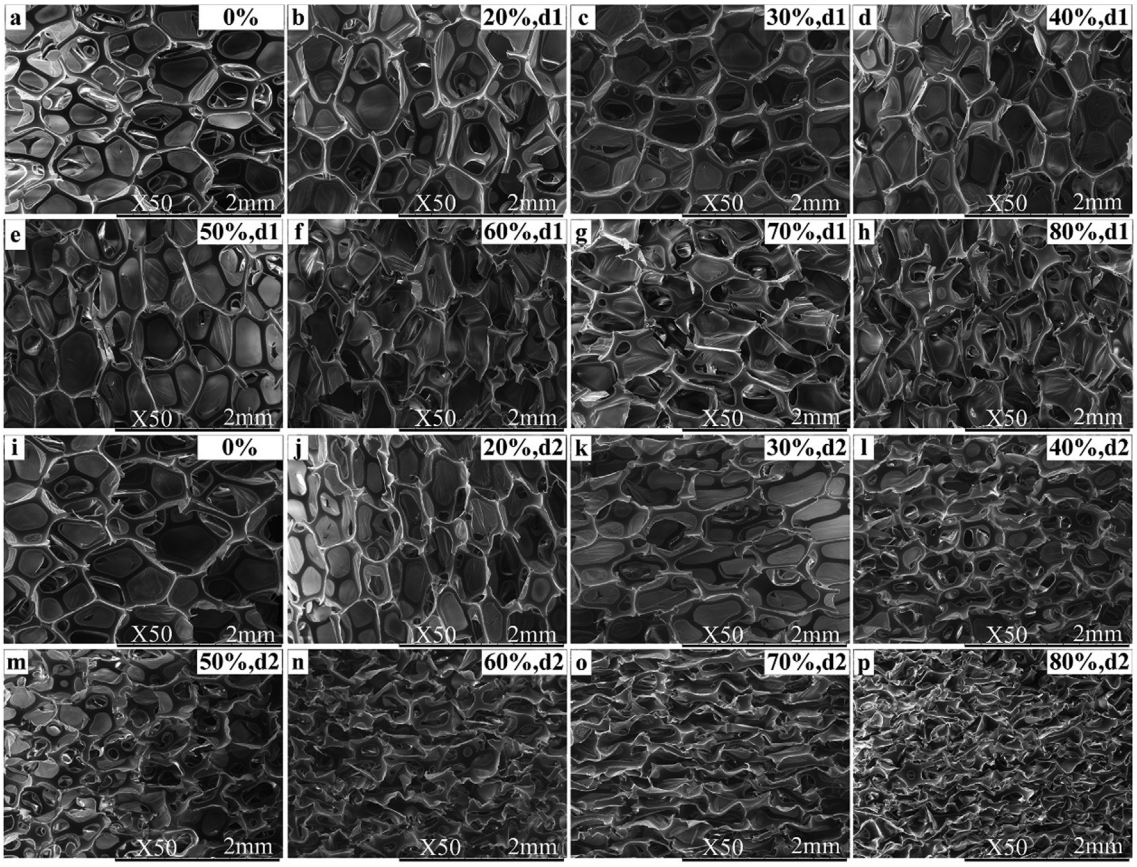

Fig. 2. SEM images of the pristine foam (a), (i) and auxetic foam with different thermoforming compression ratio r_c: along direction 1 (b)-(h) and along direction 2 (j)-(p).

elongated along the direction 1, which is also observed in other works [48,55]. This is because the open cell PU foams are produced out of reactors, with the foam cells tending to align along the rise direction during the foaming process and providing a slight transverse isotropy. In comparison, the cells of the auxetic foam collapse along the uniaxial thermoform compression direction (d1), with buckled ribs tending to orient on the 2–3 plane and following shapes typical of the re-entrant microstructure in auxetic porous materials [37]. As r_c increases, the inner microstructures of the auxetic foam becomes denser and the tortuosity of the curved ribs becomes more obvious.

The skeleton models of the different foam specimens are obtained by extracting the centerline of the ribs from the processed 3D models [58,60] using the custom module provided by the Avizo software. Compared with the original 3D model, the skeleton model can provide more quantitative information about the topological characteristics of the foam. The skeleton models of different foams are shown in red in Fig. 4 (d)-(f). The skeleton representations overlap with the processed 3D models (blue color) quite well. Statistical distributions of the topological characteristics of the foams are obtained from the skeleton models using a series of MATLAB codes. Due to the limitation of the skeletonization algorithm, the skeleton models may contain some tiny segments at places where the rib joints are too large. Tiny segments with length less than 0.05 mm are therefore ignored when conducting the statistical calculation.

The probability density functions (PDF) of the length, mean diameter and tortuosity of the ribs are shown in Fig. 5 (a), (b) and (c). The calculation of PDF f_n is defined as:

$$f_n = \frac{L_{rib-n}}{L_{rib-all}\Delta\alpha} \tag{1}$$

In (1), L_{rib-n} is the sum of length of the ribs with parameters distributed within the n^{th} interval; $L_{rib-all}$ is the sum of length of all the ribs in the skeleton model; $\Delta\alpha$ is the width of parameter interval for the PDF and the parameter can be rib length, mean diameter and tortuosity respectively. The tortuosity of the ribs is defined as:

$$\tau = \frac{C}{L} \tag{2}$$

In (2), C is the length of the curved rib and L is the distance between two ends of the rib [69]. The distributions of the rib length and its mean diameter are quite similar for different auxetic foam specimens, which indicates that the thermoforming compression procedure only curves the ribs without providing significantly damage or failure to them. Those distributions are also close to the normal one and mainly concentrate at ~0.3 mm and 0.03 mm respectively. The difference of rib tortuosity between the different foams is quite evident. The rib tortuosity of pristine foam is almost equal to 1, i.e. a straight line. As the volumetric compression ratio increases, more ribs are curved, thus the tortuosity of increasing numbers of ribs is larger than 1, compared with the pristine foam.

The volume fraction of the ribs at each cross section of the specimen is defined as:

$$p_n = \frac{A_{rib-n}}{A_{all-n}} \tag{3}$$

In Eq. (3) A_{rib-n} is the area of the ribs at the n^{th} cutting section A (Fig. 3); A_{all-n} is the area of the specimen cross section. It is shown in Fig. 5 (d) that p_n values from different foams are almost constant along the height direction of the specimen, although those values tend to fluctuate especially for the pristine foam and the 30% compression ration auxetic foam due to their sparse internal structure

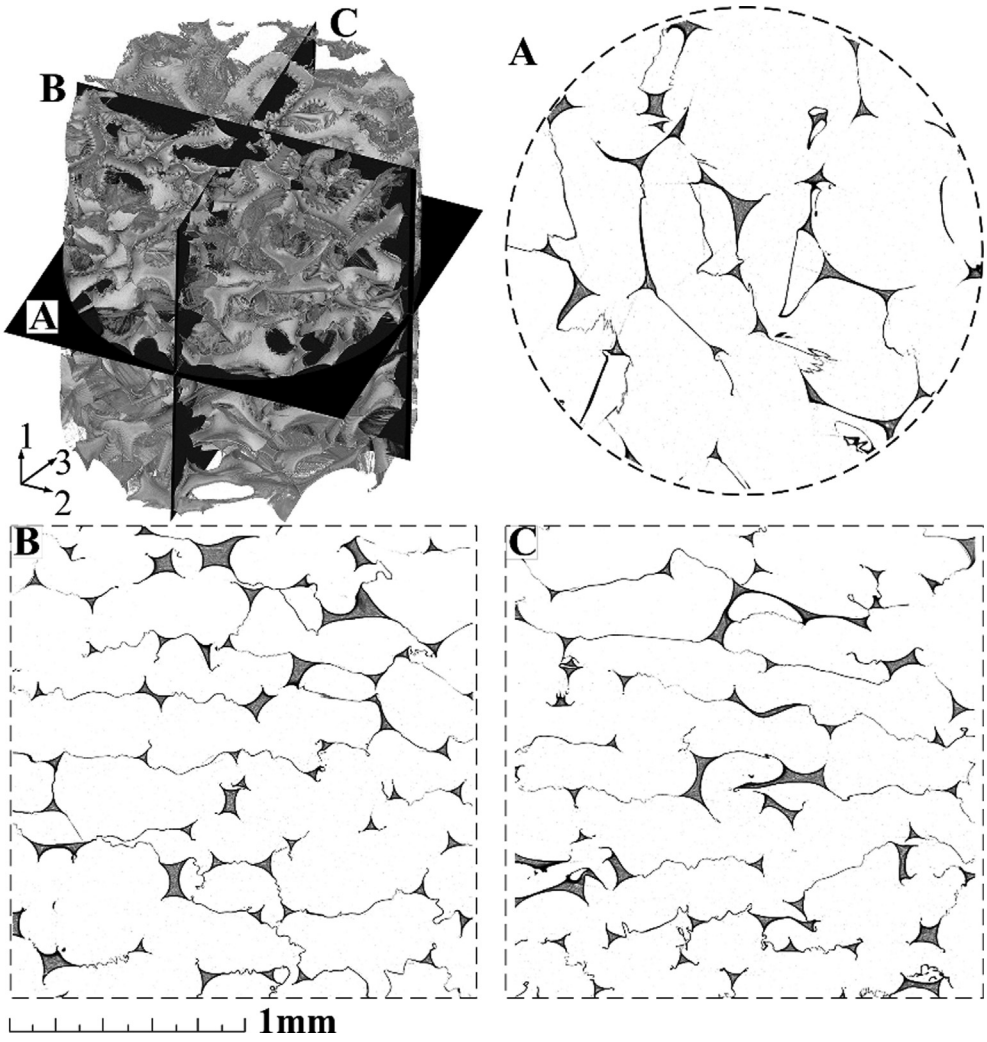

Fig. 3. Three-dimensional model and sections of the auxetic foam with r_c = 60% along the different directions.

and the small CT scan volume. The p_n of pristine foam, 30% and 60% auxetic foam are around 0.030, 0.041 and 0.069 respectively in Fig. 5 (d). The measured densities of the 3 types of foams are 27.0, 33.6 and 62.4 kg/m^3. The density of the PU solid extracted from inverse identification is 900 kg/m^3, within the wide range of 500–1220 kg/m^3 from open literature [70]. The 900 kg/m^3 is valid if one assumes that the volume fraction 0.029 of the pristine foam extracted by CT data is a reliable figure. The resulting volume fractions of the auxetic foams with r_c = 30% and 60% are 0.037 and 0.069, which are close to the results of p_n from the CT data.

The rib orientation distribution map [58] describes the orientation of all ribs inside the foam. To build this map all the line segments in the foam skeleton model are firstly projected along a vector **g** with spatial angle θ_2 and θ_{2-3} , which represent the angles against axis 2 and plane 2–3 (Fig. 6 (a)). The sum of all projected line segments l_n along **g** is calculated from Eq. (4). By changing the orientation of the vector **g**, the projections along all spatial directions can be obtained and then normalized using Eq. (5).

$$S_g = \sum_{n=1}^{N} |l_n'| \tag{4}$$

$$q_g = \frac{S_g}{S_{\min}} \tag{5}$$

The rib orientation distribution map of the pristine foam and the 30% and 60% compressed auxetic foams are shown in Fig. 6 (b), (c) and (d). The pristine foam has more ribs oriented along direction 1, the rise direction of the foam during manufacturing in reactor, which has also been observed in the previous described 3D model (Fig. 4 (d)). One can also notice a slight anisotropy of the orientation of the ribs in the 2–3 plane, with a marginally lower number of ribs distributed along the direction θ_2 = 130°. In comparison, the auxetic foam has more ribs oriented within the 2–3 plane and less ribs along the thermoforming compression direction 1. More ribs in the 2–3 plane are distributed along the direction θ_2 = 130°, showing anisotropy. This is because the thermoforming compression direction for manufacturing the auxetic foam is the lateral direction 2 of the pristine foam (Fig. 4 (d)). Therefore, the rising direction 1 of the pristine foam is located within the transverse 2–3 plane of the auxetic foam, resulting in the slight anisotropy of the auxetic foam within the same 2–3 plane.

4. Quasi-static experimental tests

4.1. Test rig

The quasi-static test rig for compressive and tensile tests of the foam specimens is shown in Fig. 7. The tests have been per-

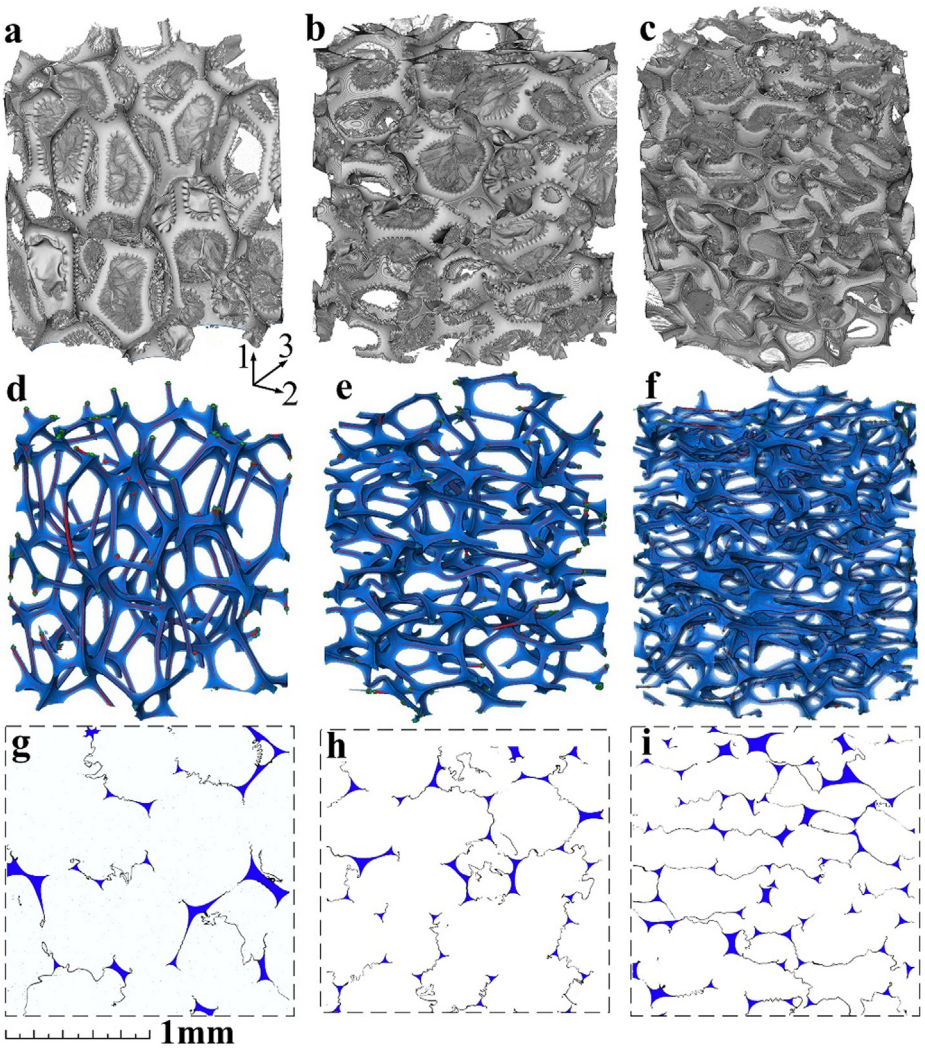

Fig. 4. 3D models, processed and skeleton models and vertical sections cut by plane 1–3 of the pristine foam (a), (d), (g); auxetic foam with r_c = 30% (b), (e), (h) and 60% (c), (f), (i).

formed using a single column tabletop system (Instron, type 3343) with a 1 kN force sensor (Instron, model 2519–105). A dual-camera video gauge system (iMETRUM Limited, camera type CAM 13) has been used to measure the strains and Poisson's ratios along two orthogonal lateral directions [46]. The Poisson's ratio used here is defined as $v_{xy} = -\varepsilon_y/\varepsilon_x$, where ε_x and ε_y are the nominal strains along the vertical loading and transverse horizontal directions, respectively [46]. The layout of the strain measuring points is shown in Fig. 7 (c) and (d). Three parallel points are used for the average of each strain measurement, without large deviations in most cases. In order to exclude boundary effects from the results, only the central 50% of the tensile specimen along the uniaxial loading direction has been used here to measure the strain for the extraction of the modulus and Poisson's ratios. During the compressive test, only the 30% central part of the specimen has been used to determine the Poisson's ratio. This is because the wrinkling and inhomogeneous deformations in the auxetic foams (Fig. 7 (b)) during compression make the strain measurements not reliable over large sections. The displacement of the top compression plate is used to estimate the compressive modulus of the foam, because the buckling of the ribs under compression may occur near the top and bottom boundaries of the specimens. This may result in slightly inhomogeneous axial deformations [71].

The PU foam material is viscoelastic and the modulus decreases gradually with the decreasing loading rate till a constant value [72,73]. In preliminary tests, it is found that the modulus of the PU foam is almost constant when the loading rate reduces to ~3 mm/min. The compressive and tensile tests have been therefore carried out in displacement control with a loading rate of 2 mm/min, slow enough to approximate a quasi-static testing regime. A preload of 1 N for the compressive tests and of 0.5 N for the tensile ones have been applied to obtain a stable initial testing state and avoid sources of potential errors like unparallel top and bottom surfaces of the specimens (especially during the compressive tests). Due to the Mullins effects in the PU material [74,75], the first few loops of the quasi-static cyclic loading–unloading tests show different mechanical properties. Not until the 4th loop the experimental results start to converge and maintain stability [46,74]. Five loading–unloading cycles have been therefore performed for each specimen, and only the 5th loop has been used to evaluate the properties of the material. The Mullins effect also results in residual strains caused by the first 4 loops along both axial and transverse directions [74,75], which should be eliminated when calculating the modulus and Poisson's ratio. The loss factor is computed from the hysteretic loops by using equation, where ΔW is dissipated energy within one hysteretic loop and U is the corresponding elastic energy stored in the material [76].

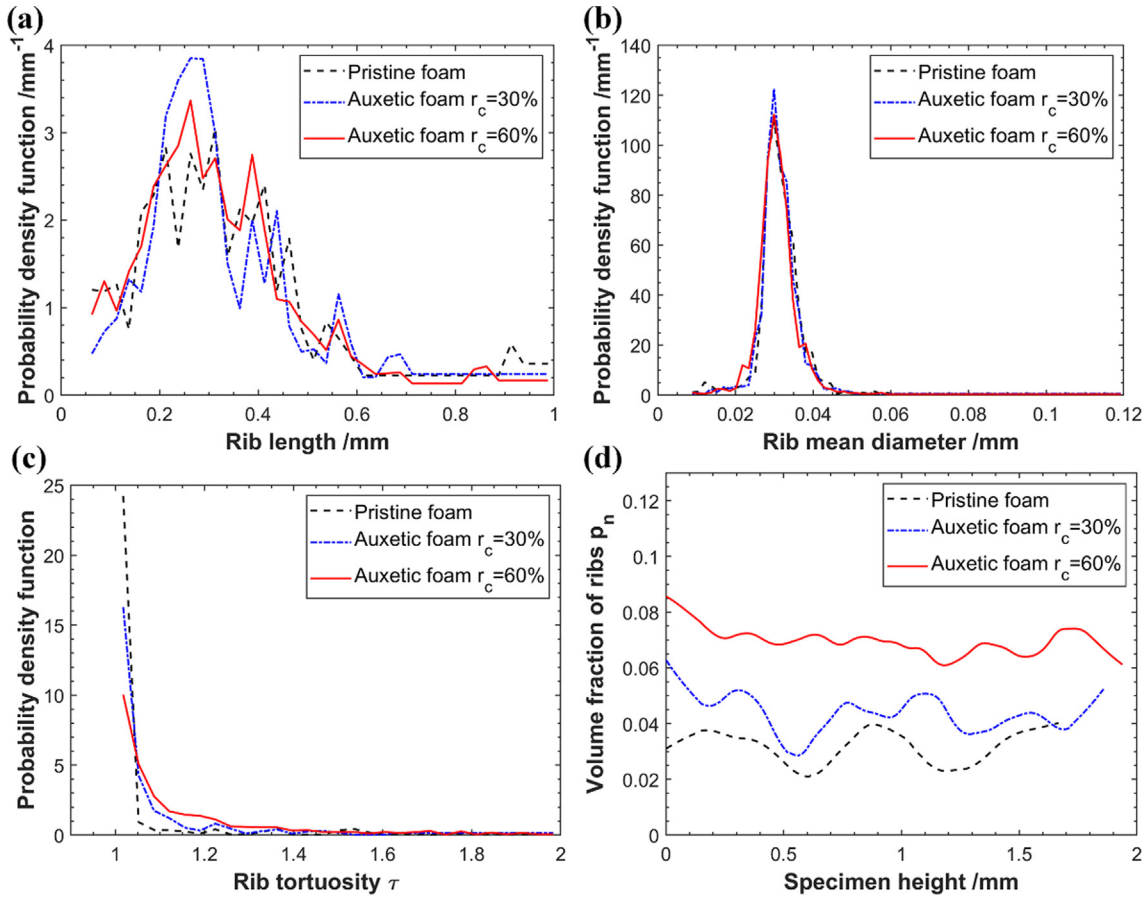

Fig. 5. Topological parameters of different foam specimens: probability density function of the length (a), mean diameter (b) and tortuosity (c) of ribs inside different foams; volume fraction of the PU in each 2–3 section versus specimen height (d).

$$\eta = \frac{\Delta W}{2\pi U} \tag{6}$$

4.2. Tensile test results

The hysteretic loops associated to tensile loading of the sample No. 1 for foams with different r_c are shown in Fig. 8 (a). There are three parallel specimens for each type of foam. The two T2 and one T1 types as described in Fig. 1 (c) show no large deviations, as illustrated by the error bars present in Fig. 8 (b)-(f). This indicates that the difference of width and depth of the specimen along the thermoforming and transverse directions affects only slightly the mechanical properties of the foams. So only the hysteretic loops of No.1 sample are given in Fig. 8 (a), without repeating the similar results from No. 2 and 3 samples. The maximum tensile strain for all specimens along the d2 direction is 0.2. The residual deformation of the specimens can be observed after the tensile tests, therefore the 5th hysteretic loop always starts from a residual strain and ends at a nominal strain of 0.2. After shifting the 5th hysteretic loop to start at the origin of the coordinates, the maximum strains are reduced to ~0.12. Fig. 8 (a) shows that all hysteretic loops have a similar shape and the slope of different loading curves mostly increases with the value of r_c, although the difference between auxetic foams with compression ratios ranging from 20% to 60% is not significant.

The strain-tangent modulus of different foam specimens is shown in Fig. 8 (b). All curves show similar trends. The tensile tangent modulus E_{t2} decreases first with the strain until ~0.01, with a stable plateau up to ~0.05 strain and a final gentle increase. The first decrease of E_{t2} at small strains is mainly caused by the behavior of the polyurethane material due to the Mullins effects in cyclic loading, which has also been observed elsewhere [46]. The final gentle increase of E_{t2} after 5% of strain is mainly caused by the elongation of the cells under tension, which will be discussed further in following FEM simulation results (Section 5). The moduli of the auxetic foams with r_c ranging from 20% to 60% cluster together around 0.5 MPa, higher than the pristine foam but lower than the 70% and 80% auxetic foams. The E_{t2} of the different foams at 0.05 strain are extracted from Fig. 8 (b) and plotted versus r_c in Fig. 8 (e). The E_{t2} modulus increases slightly first, from 0.26 MPa of the pristine foam to a plateau of ~0.43 MPa with r_c ranging from 30% to 60%. The moduli then feature a sharp rise to 1.1 MPa at r_c = 80%. The loss factors of the different foams are plotted versus r_c in Fig. 8 (e). The loss factor fluctuates around 0.04, showing no obvious dependency on the compression ratio. It can also be observed from Fig. 8 (b) that the error associated to E_{t2} rises as the compression ratio r_c increases. This is because that the density of the auxetic foam increases with the compression ratio r_c. More contacts and interconnections between the ribs are present due to the uniaxial thermoforming compression when r_c increase to 70%-80% (see also Fig. 2 (o) and (p)). The tensile loading can cause detachment of the intertwined ribs and the breaking of the weaker cell ribs inside the auxetic foams. Therefore, the auxetic foams with larger r_c, and containing more interconnections between inner ribs show a more obvious instability during tensile loading.

The Poisson's ratio ν_{21} and ν_{23} of the different foam specimens under tension along d2 are shown in Fig. 8 (c) and (d). Both ν_{21} and ν_{23} increase slightly with strain. ν_{21} declines with r_c, reaching

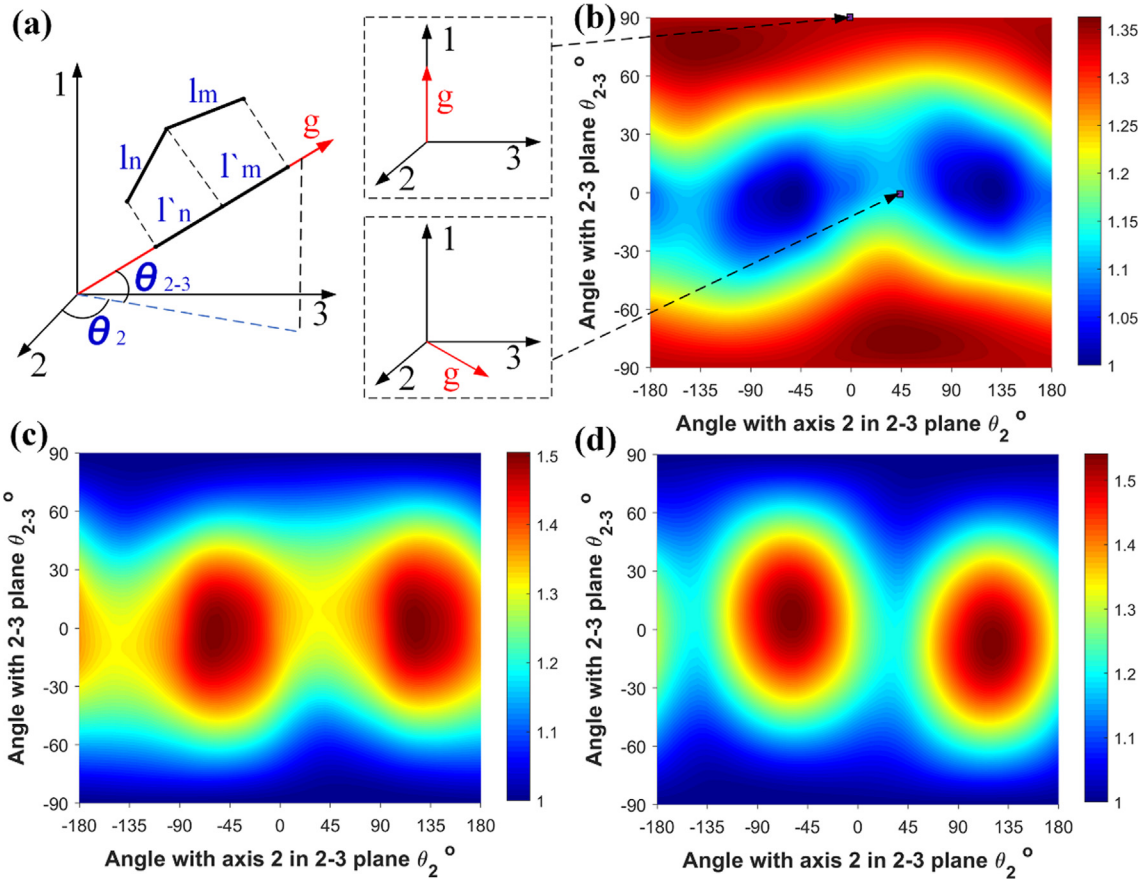

Fig. 6. Schematics of the projection of the segments (a) and the orientation distribution map of ribs in different foam specimens: pristine foam (b), auxetic foam with r_c = 30% (c) and 60% (d).

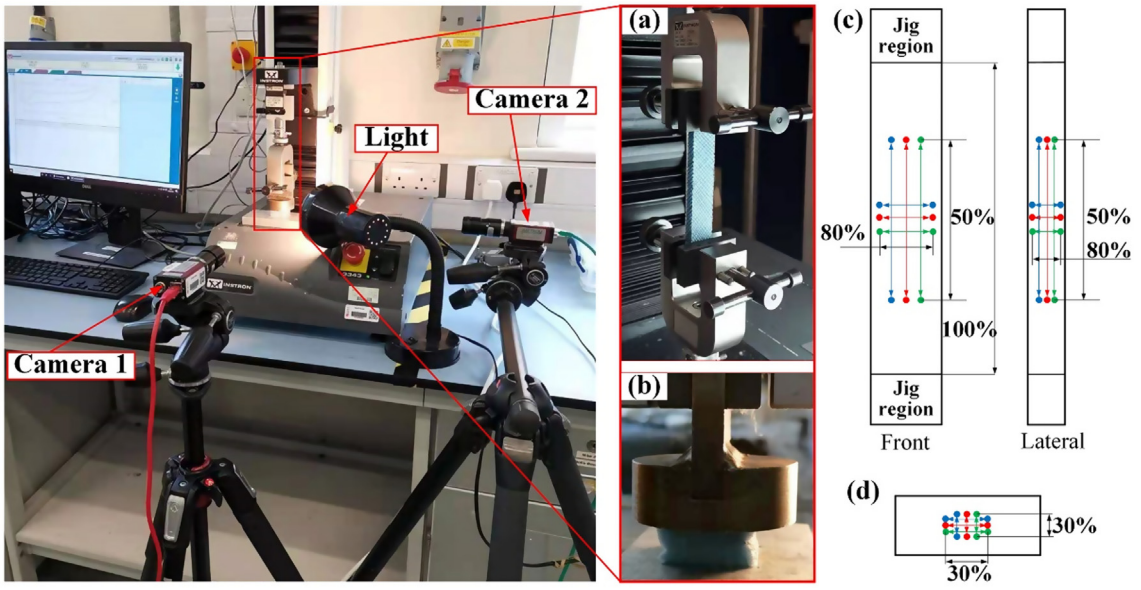

Fig. 7. Test rig of quasi static experiments and the layout of Poisson's ratio measurement: (a), (c) tensile test and (b), (d) compression test.

negative values when r_c > 40%. In comparison, the Poisson's ratio v_{23} of both pristine and auxetic foams is within 0.2–0.8, showing no auxeticity. The v_{21} and v_{23} of the different foams at 0.05 strain are obtained from curves in Fig. 8 (c), (d) and then plotted in Fig. 8 (f) to show the effect of the volumetric compression ratio on the Poisson's ratio. It can be observed that v_{21} decreases monotonously with r_c, from ~0.5 of the pristine foam to ~0 (r_c = 40%), and then finally around −0.9 (r_c = 80%). On contrary, v_{23} increases slightly first, from 0.5 to 0.75 as r_c increased to 20% and then gently decreases to 0.3 for larger r_c values. The auxetic phenomenon only

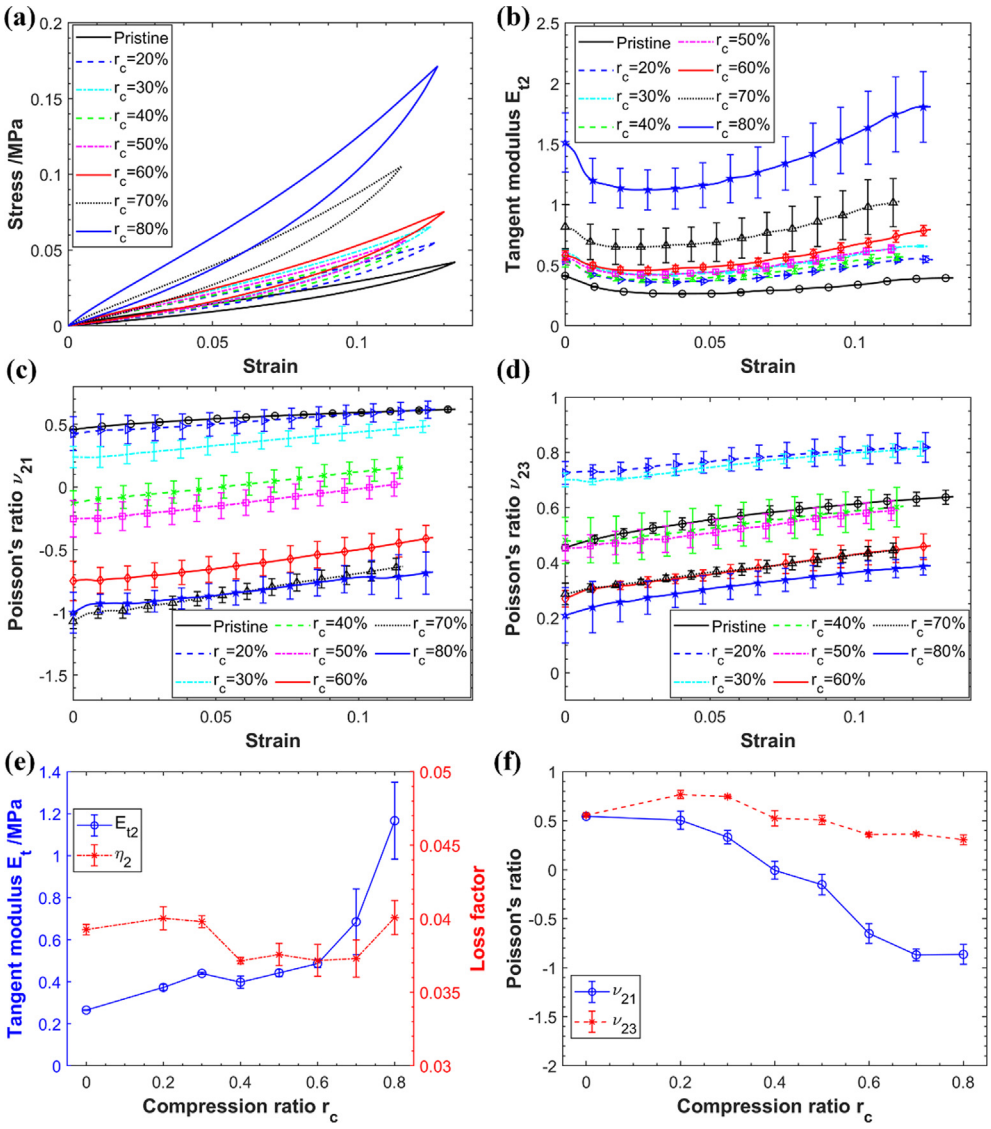

Fig. 8. Tensile test results for the auxetic foam loaded along the d2 direction with different thermoforming compression ratio r_c: hysteretic loops (a); tangent modulus (b) Poisson's ratio ν_{21}(c) and ν_{23}(d) of loading procedure; modulus, loss factor (e) and Poisson's ratios (f) at 5% strain versus r_c.

appears to exist along the thermoforming compression direction d1 when loaded along the transverse d2 direction, without any auxeticity along d3. The auxeticity in the 1–2 plane is caused by the re-entrant cell structures provided by the buckled ribs during thermoforming, however the convexity of the cell microstructures in the 2–3 plane is limited, as shown in Figs. 2 and 4. Consequently, the Poisson's ratio ν_{21} can reach negative values while ν_{23} is always positive. The deformation mechanism will be discussed further in Section 5 when discussing the FEM simulations.

4.3. Compressive test results

Compressive tests along the d1 and d2 directions were carried out on the foam samples C1 and C2 (Fig. 1 (c)). The hysteretic loops of the No. 1 sample of foams with different r_c values loaded along the d1 and d2 directions are shown in Fig. 9 (a) and (b). The maximum compressive strain here is 0.1 and only a 0.08 strain remains after eliminating the residual strain. The slopes of the strain–stress curves for the 80% compression ratio foam are obviously significantly higher than those of other foams along both the d1 and d2 directions, with higher stress along d2. The hysteretic loops of the auxetic foams with r_c ranging from 20% to 70% are all clustered together, with values lower than those of the pristine foam when tested along the d1 direction. In contrast, the loops of the auxetic foams along d2 are all located above those of the pristine foam, with the slope of the curves obviously increasing with r_c. Besides, the hysteretic loops of the pristine foam along d1 show a bilinear shape during loading, which is visibly different from that along the d2 direction.

The tangent modulus derived from the loading curves are illustrated in Fig. 9 (c) and (d). The modulus of the 80% auxetic foam is much larger than the one of the other foams along both the d1 and d2 directions. The E_{t2} of each auxetic foam is always higher than its E_{t1} counterpart, showing therefore a significant transverse isotropy. The E_{t1} of the 70% and 80% auxetic foams decreases first slightly at small strain ranges (<2%) due to the Mullins effect and initial slack of the testing rig. The modulus then increases gently with strain, something which is different from the decline of the E_{t1} and E_{t2} moduli versus the strain in the other cases. This is because the compression of auxetic foams with large r_c values along the d1 direction will generate more contacts between the ribs inside the dense porous configurations, thus resulting in an

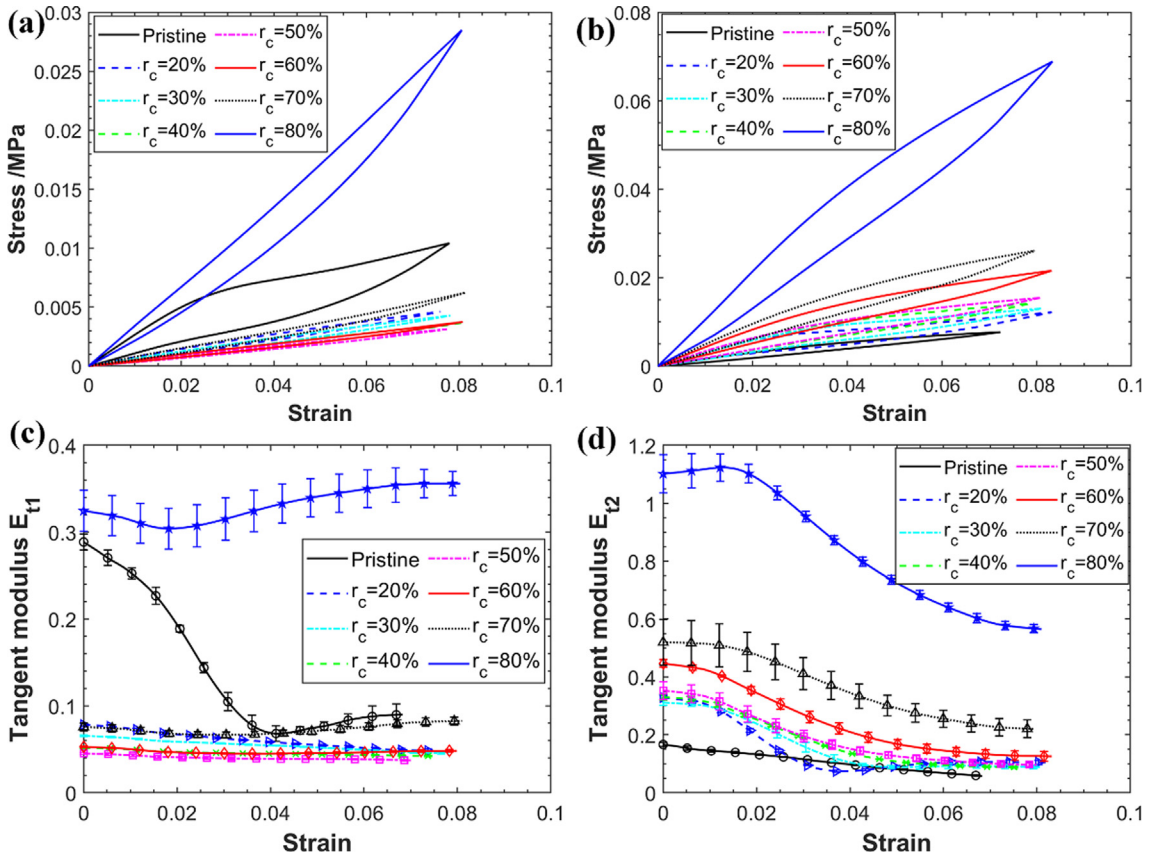

Fig. 9. Compressive test results of the auxetic foam with different thermoforming compression ratio r_c along different directions: hysteretic loops and tangent modulus along d1 direction (a) (c) and d2 direction (b) (d).

increase of the modulus versus the strain. As for the foams with small r_c values, the resultant low density and sparser inner structures make the contact between ribs under compression along the d1 direction less pronounced within small to medium strain ranges (<10%). When compressed along d2 of all foams or d1 of foams with low r_c, the geometry nonlinearity of the bending of the cell ribs under compressive loading plays the dominant role, with a resulting decrease in modulus with strain. These deformation mechanisms will be further analyzed when looking at the FEM results.

The E_{t1} values of the auxetic foams with volumetric compression ratios ranging from 20% to 70% are always lower than those of the pristine foam, while the E_{t2} values are – on the contrary - always larger than those of the conventional foam. It can be also noticed that the E_{t1} modulus of the pristine foam decreases significantly from 0.28 MPa to 0.07 MPa at 0.04 strain and then slightly increases to 0.09 MPa, compared with the slow decrease from 0.17 MPa to 0.09 MPa of the E_{t2} modulus. This is because direction 1 is the one associated to the foam rising during manufacturing, with cells and pores elongated along this direction (Fig. 4 (d)). The ribs oriented along the d1 direction provide higher stiffness at small strains under loading along the d1 direction compared with the d2 one. Those ribs are however easier to buckle at higher compressive strains, resulting in a significant reduction of the E_{t1} modulus for the pristine foam.

The Poisson's ratios ν_{13} , ν_{12} , ν_{23} and ν_{21} of the different foams versus the compressive strain are shown in Fig. 10 (a)-(d). When loaded along the thermoform compression direction (d1), the ν_{13} and ν_{12} of the auxetic all keep constant around 0 for increasing strains; the ν_{13} and ν_{12} of pristine foam are however always around 0.41. When compressed along the transverse direction (d2), the performance of ν_{23} and ν_{21} are quite different. The ν_{23} of different foams are always positive, ranging between 0 and 1 according to the volumetric compression ratio and in most cases decreases gently with the strain. In comparison, the ν_{21} of auxetic foams with r_c values ranging from 30% to 70% are negative and decrease slowly with the strain. This indicates that the auxetic foam only exhibits auxeticity in the 1–2 plane with compressive loading along the d2 direction due to its transverse isotropic microstructure, similarly to what has been observed during tensile loading. It must be noted that the ν_{21} value of the 80% auxetic foam under tension is −0.9, compared to the positive 0.5 in compression. A similar phenomenon has also been observed in other auxetic porous materials with high density [46]. This is because the widely distributed contacts between interconnected ribs of high-density auxetic foam prevent the sample from a lateral shrink under uniaxial compression along the d2 direction, so no auxeticity is observed. On the contrary, the lateral expansion of auxetic foams with high r_c values and subjected to uniaxial tension along the direction d2 can reduce the equivalent density and the number of contacts inside the re-entrant cell structures, so auxeticity can be here detected.

Besides, the larger scattering of the Poisson's ratios obtained under compression along the d2 direction is more evident than in the case of the PR values obtained from tensile tests along d2, or compressive tests along d1. This is because the wrinkling and twisting deformation on the boundaries of the auxetic foam samples under compression along d2 (Fig. 7 (b)) make the strain measurement by video gauge through the surface points not as reliable as in the case of the tensile tests. The wrinkling and twisting of the samples at the boundary also make the deformation of the internal cells somewhat inhomogeneous.

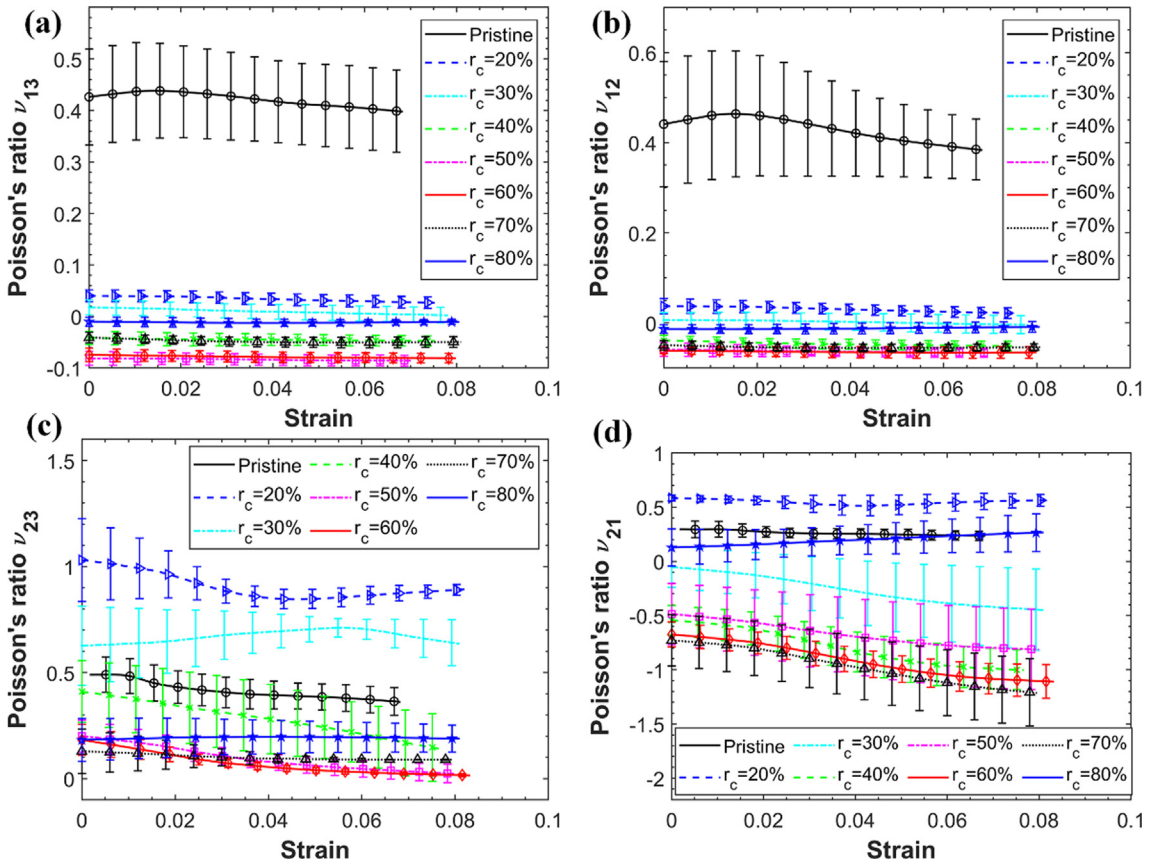

Fig. 10. Poisson's ratios of the auxetic foam along different directions in compressive test: ν_{13}(a) and ν_{12}(b) compressed along d1 direction; ν_{23}(c) and ν_{21}(d) compressed along d2 direction.

The tangent modulus E_{t1} and E_{t2} of the different foams at 0.05 of compressive strain are shown in Fig. 11 (a). The E_{t2} modulus is always larger than the E_{t1} one for all auxetic foams here considered. The E_{t1} decreases slightly from 0.07 MPa (r_c = 0%) to 0.04 MPa (r_c = 50%), and then rise gently to 0.07 MPa (r_c = 70%), with a final jump to 0.34 MPa (r_c = 80%). In comparison, the modulus E_{t2} increases first from 0.08 MPa (r_c = 0%) to 0.17 MPa (r_c = 60%) and then sharply to 0.72 MPa (r_c = 80%). The compressive loss factor η_2 is always larger than η_1 for all auxetic foams. The loss factor η_2 decreases first slowly from 0.054 (r_c = 0%) to 0.038 (r_c = 50%) and then keeps constant versus r_c. The η_1 keeps constant at around 0.02 with r_c ranging from 20% to 70%, and finally rises to 0.029 as r_c increases to 80%.

The Poisson's ratio along the different directions of the foams at 0.05 compressive strain are extracted from Fig. 10 and shown in Fig. 11 (b). The values of ν_{12} and ν_{13} decline from the 0.41 of the pristine foam to ~0 for the auxetic foams and is almost constant with the volumetric compression ratio. In contrast, the effect of r_c on ν_{21} and ν_{23} is more significant. The value of ν_{23} is always positive, fluctuating between 0.04 and 0.85. The ν_{21} is above 0 when r_c < 20%, and then reduces to −0.34 (r_c = 30%), following by a plateau of ~−1 (r_c ranging from 40% to 70%) and a final sharp increase to 0.21 (r_c = 80%). This indicates that only the auxetic foams with r_c ranging from 30% to 70% exhibit auxeticity within in the 1–2 plane during compression tests.

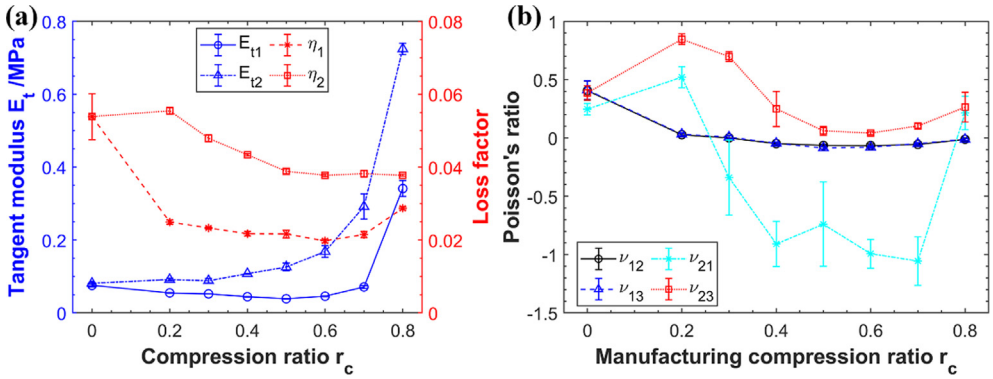

Fig. 11. Tangent modulus, loss factor (a) and Poisson's ratios (b) at 5% strain versus r_c along different compression directions.

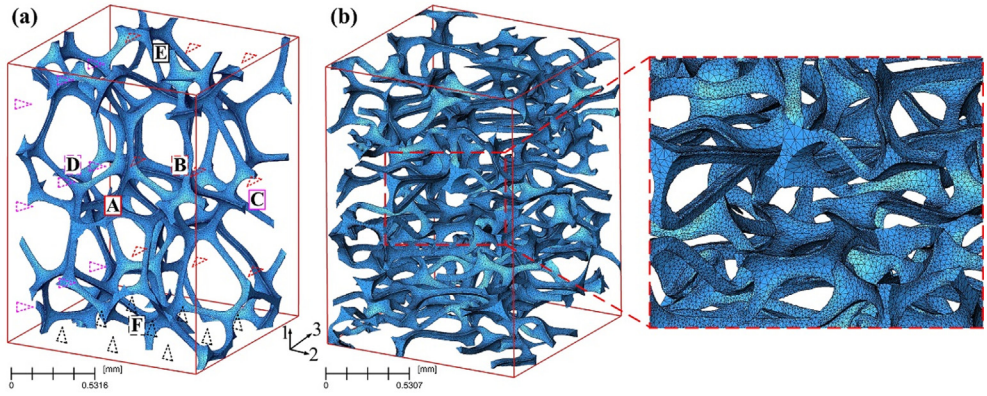

Fig. 12. Finite element models of the pristine (a) and the auxetic foam with r_c = 60% (b).

5. Finite element simulation of the deformation behavior

Cuboid-shaped 3D models of the pristine and 60% auxetic foams with sizes of 1.37 × 1.37 × 1.86 mm have been extracted from the cylinder-shape processed 3D models (Fig. 4 (d) and (f)) and then meshed using tetrahedral solid elements using Avizo. The FE models of the pristine and auxetic foams with r_c = 60% are shown in Fig. 12 (a) and (b). The models contain 101,530 nodes and

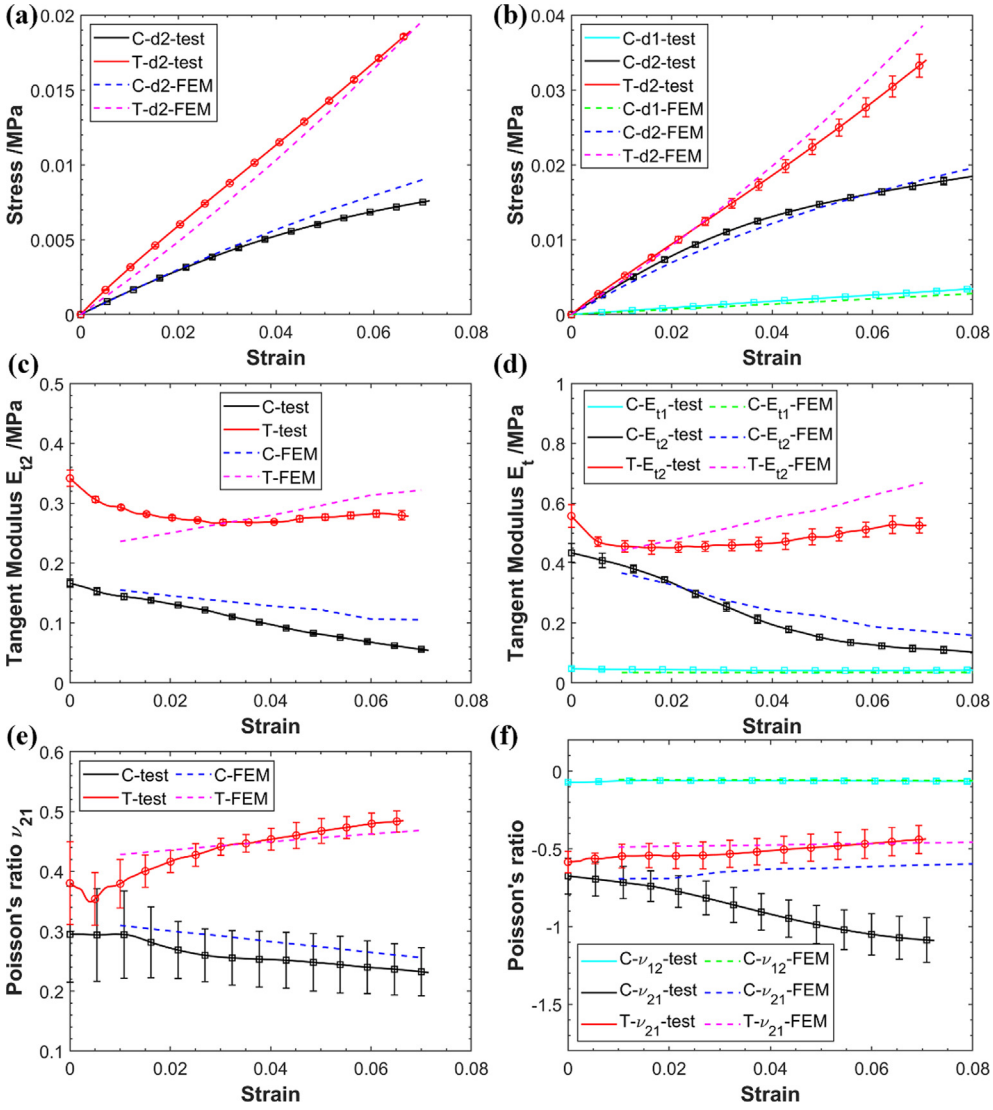

Fig. 13. Comparison between experimental and numerical results: strain–stress curve during loading, tangent modulus and Poisson's ratio of the pristine (a), (c), (e) and 60% auxetic foam (b), (d), (f) respectively. The C and T in the legends represent compression and tension, respectively.

275,200 elements (pristine foam) and 308,594 nodes and 858,992 elements for the auxetic type. The boundary conditions applied to the cuboid FE model form a quadrant representative volume element (RVE) model [77,78], as shown in Fig. 12 (a). All nodes on the three orthogonal surfaces B, D and E are fixed along the perpendicular direction of each surface. All nodes at A, C, E are coupled with same displacement, vertical to the surface. Perpendicular displacements are applied to the surfaces A, C or E as needed for the load case and then the total reaction force and transverse displacement can be extracted to calculate the modulus and the Poisson's ratio using ANSYS 15.

The modulus of the core PU material is set as 260 MPa, which is obtained inversely by fitting the FEM to the pristine foam specimen tests. The modulus of the PU used in this FE model is slightly higher than the upper range of 10–250 MPa (strain < 20%) in Refs. [46,72,79,80], because the elimination of the membranes weakens the stiffness of the FE model compared with the one of the real foam, and therefore needs to be compensated using a slightly larger modulus for the PU. The nonlinearity of the PU material can be here neglected because the maximum strain of the foam specimen under simulation and experiments are within 10%, far lower than the linear elasticity limit of the PU material [72,79]. Geometric nonlinearity and contact between elements and surfaces have been considered in these FEM simulations. The distribution of ribs inside the model is quite sparse and the maximum strain applied during simulation is small (<0.1). During the calculations it has been verified that almost no contact occurs between ribs inside the material (see the images of the deformed cells in Fig. 14 and Fig. 15. Therefore, contacts between ribs have been ignored and no contact pair is built within the FE model.

The comparison between simulated and experimental results of the pristine and 60% auxetic foam is shown in Fig. 13. The FEM results coincide well with the experiments. The slopes of the tensile loading curves are always larger than the compressive ones, while the compressive stresses along the thermoforming direction d1 are lower than the others (Fig. 13 (a) and (b)). The compressive strain–stress curves show a slight softening effect with increasing strain. As mentioned in Section 4, the experimental results in Fig. 13 are all from the 5th loop of the cyclic loading tests and the residual strain caused by Mullins effect is eliminated by shifting the strain–stress curves to start at the origin of the graph. Therefore, the maximum strain in Fig. 13 is ~0.07 for the pristine foam and ~0.08 for 60% auxetic foam, lower than the applied maximum strain of 0.1 in experiment. The residual strain changes the shape of the foam cells, affecting the accuracy of the FE model and needs to be considered when commenting the FEM simulations. We have therefore eliminated the initial portions (3% of strain for the pristine and 2% for the auxetic) of the simulated strain–stress curves. The remaining parts of the numerical strain–stress curves are shifted to start at the origin of the graph; the calculation of the numerical tangent modulus and the Poisson's ratios takes also into account the elimination of the residual strain.

Numerical and experimental values for the tangent modulus of the pristine and 60% auxetic foams are shown in Fig. 13 (c), (d). The tensile modulus is always larger than the compressive one for the two types of foams. The tensile modulus gently increases with the strain, while the compressive modulus decreases in a more notice-

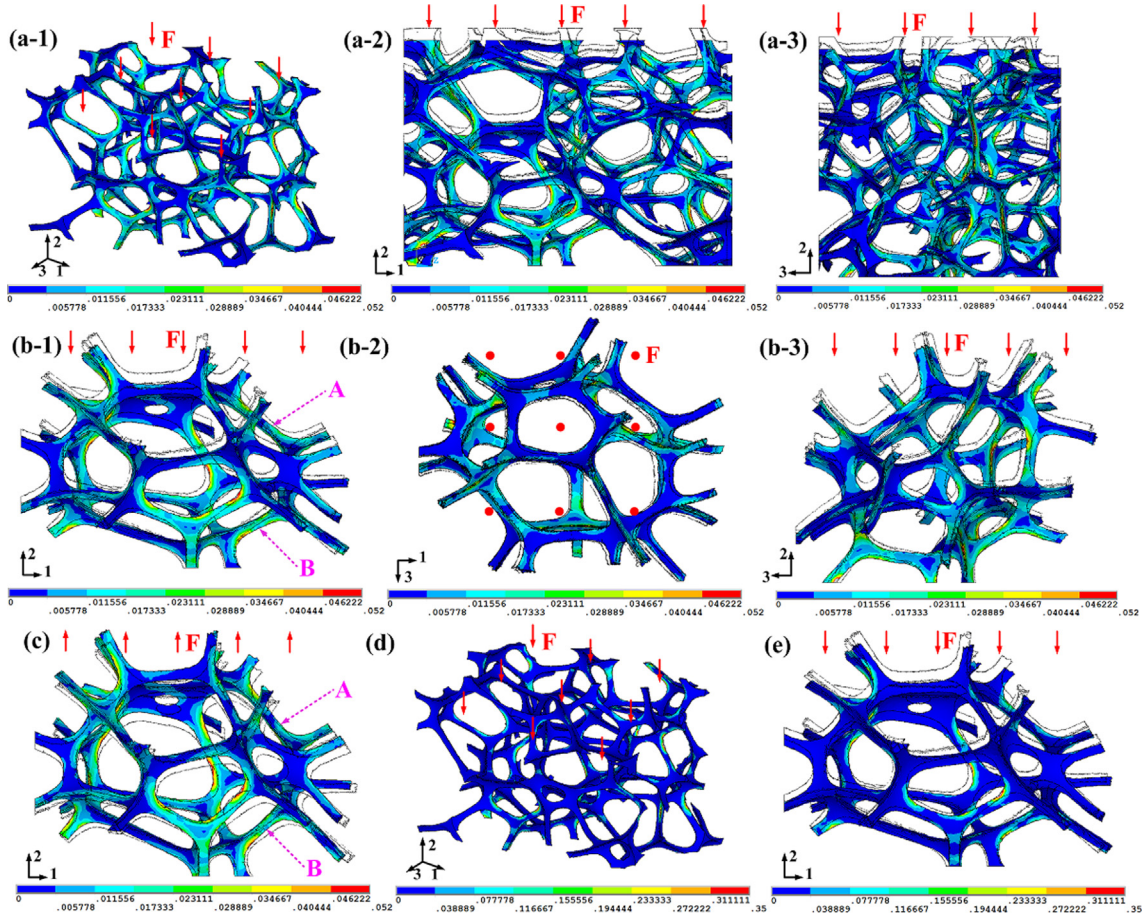

Fig. 14. Simulated von Mises strain distribution in the pristine foam sample (a) and one cell of the sample (b) under compression and tension (c) along d2; the strain energy distribution inside the whole pristine foam sample (d) and one cell (e) with compression along d2.

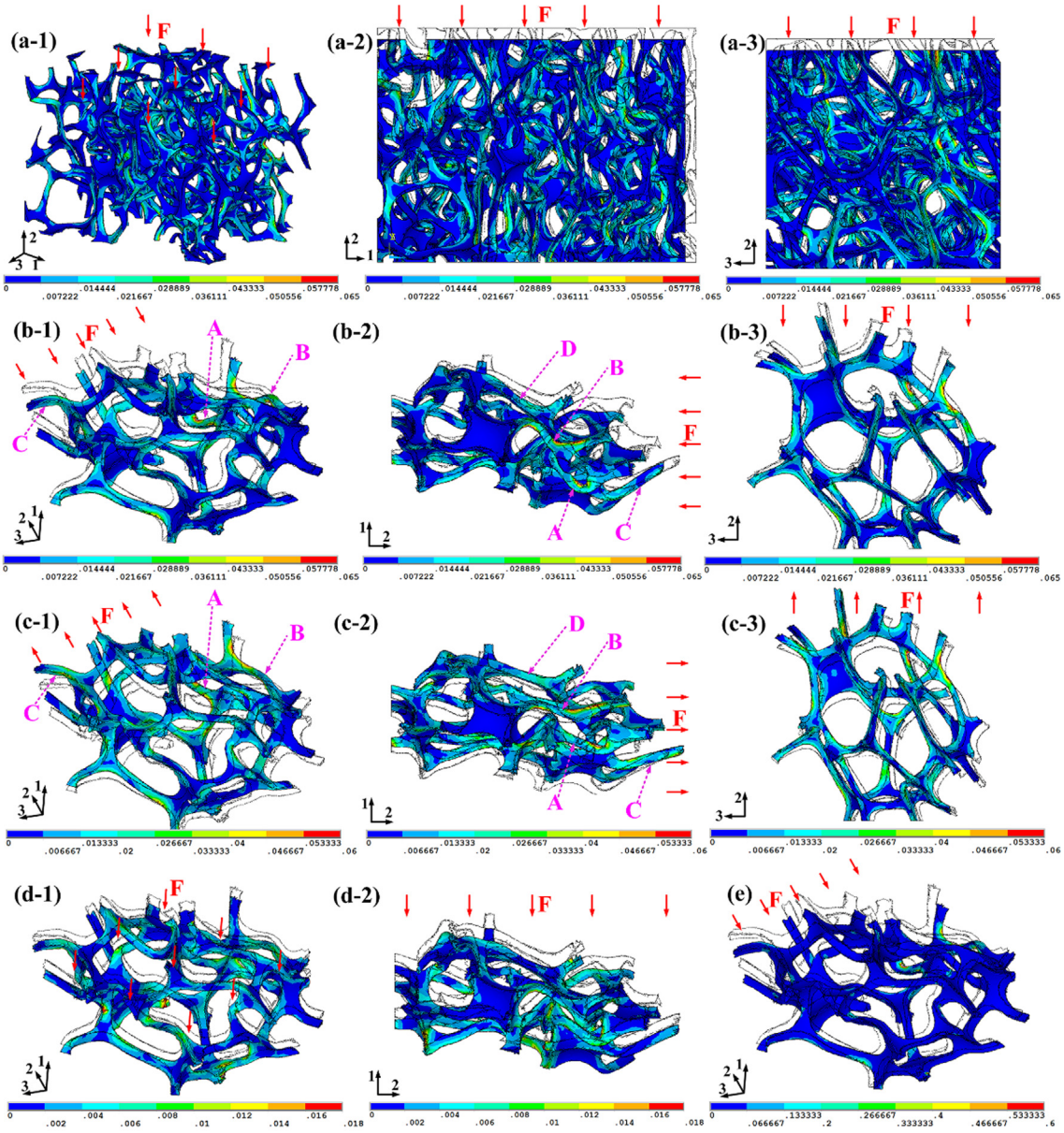

Fig. 15. Simulated von Mises strain distribution in the 60% auxetic foam sample (a) and one cell of the sample (b) under compression along d2, tension along d2 (c) and compression along d1 (d); the strain energy distribution in the cell with compression along d2 (e).

able way. The variation of the modulus versus the strain is larger in the case of the auxetic foam than the pristine one. The compressive modulus along the d1 direction is also much lower than the other moduli and is almost constant with the strain. The variation of the modulus versus the strain is similar to the one experimentally shown by the other auxetic foams (see Figs. 8 and 9).

The effect of the type of loading and strain on the tangent modulus can be appreciated by looking at the deformation mechanism of single cells inside the foams (Figs. 14 and 15). The compressive load on the pristine foam makes the inclined ribs (ribs A and B in this case) more perpendicular to the loading direction, reducing the stiffness of the cell structure (Fig. 14 (b) and (c)). In comparison, the tensile load will elongate the cell structure and make the inclined ribs to orient themselves closer to the loading direction, enhancing the stiffness of the cell. The curved ribs inside the cell of the auxetic foam, such as the rib A and B in Fig. 15 (b) and (c), will twist more severely and provide less stiffness when compressed along the direction d2. On contrary, the curved ribs will be stretched and straightened by the tensile loading, providing higher stiffness. The different performance of inclined ribs under compression and tension (see ribs C and D in Fig. 15 (b) and (c)) also affects the stiffness versus strain, similarly to the pristine foam case. Consequently, the tensile modulus of both pristine and auxetic foams is larger than the compressive one and the modulus increases with the tensile strain rather than the reduction of compressive one. The compressive load on the auxetic foam along the d1 direction is mostly supported by the weak buckled ribs generated by the uniaxial thermoform compression, as shown in Fig. 15 (d). From Fig. 6 it is also evident that in the auxetic foam more ribs tend to be oriented along the transverse direction d2 than the thermoform compression direction d1. The modulus of the auxetic foam along d1 is therefore much smaller than along d2. The different deformation mechanism of the pristine and auxetic foam cells under compressive and tensile loads has also been observed by Chan [48] using a microscope and it also agrees with the numerical results in this work.

Numerical and experimental Poisson's ratios related to the pristine and 60% auxetic foams are shown in Fig. 13 (e) and (f). The tensile Poisson's ratios are larger than the compressive ones and increase slightly with the strain, while the compressive ones tend to gently decrease. Only the v_{21} values of the auxetic foam are negative and v_{12} is always close to 0. In most cases the numerical results coincide well with the experimental ones, except for the case of the compressive v_{21}. The experimental v_{21} values in compression decline with the strain, while the numerical ones are almost constant. As discussed in Section 4.3, a likely explanation is due to the wrinkling and twisting of the auxetic foam on the surfaces of the samples when compressed along the d2 direction (Fig. 7 (b)). Those deformations make the strain measurements by video gauge through the surface points not as reliable as those acquired during the tensile tests. Therefore, the error bars associated to the v_{21} values acquired during compression are quite large (Fig. 10 (d)) and the discrepancy between experimental and FEM results is wide because the surfaces of the foam RVEs are constrained to be parallel and the deformation is assumed homogeneous during the simulation (Fig. 15 (a)).

The auxeticity is caused by the re-entrant cell structures generated by thermoform compression procedure. When under compression along the direction d2, the re-entrant inclined ribs (ribs C and D in Fig. 15 tend to incline further into the cell and reduce the size of the cells along d1, therefore exhibiting auxeticity. In comparison, under tension along d2, the same re-entrant inclined ribs are stretched and oriented closer to the tensile loading direction, increasing the lateral size of the cell and therefore behaving as an auxetic material. This type of deformation cannot be observed in the 2–3 plane, thus no auxetic behavior appears there. When the auxetic foam is compressed along the direction d1, the buckled ribs are further twisted and rotated without an obvious change in terms of cell size along the transverse directions. This leads to a zero Poisson's ratio, as shown in Fig. 15 (d).

The von Mises strain and strain energy distribution of the pristine and auxetic foams with 0.05 strain deformation under different loading conditions are shown in Figs. 14 and 15. The maximum strain and strain energy of the pristine foam are mostly distributed adjacent to the rib joints. The maximum strain inside the pristine foam is ~0.052, very close to the 0.05 strain applied to the overall foam specimen. In the auxetic foam, the maximum strain and strain energy are mainly distributed at the ends and on the kinks of the curved ribs. The maximum von Mises strain inside the foam cells is around 0.065, when deformation of 0.05 strain is applied along the d2 for the auxetic foam sample. In comparison, the maximum strain is only ~0.018 when a global 0.05 strain deformation is applied along d1. This is because the overall twisting and rotating deformation of buckled ribs when loaded along d1 facilitate the deformation of the auxetic foam and thus eases the strain concentration at critical positions and reduces the stiffness along the d1 direction.

6. Conclusions

A simpler method to manufacture auxetic foam consisting in a single direction thermoforming compression and using an open mould has been developed here. The mechanical tests related to the auxetic foams with different thermoform compression ratios r_c show that the foam samples exhibit auxetic behavior in the 1–2 plane only when the volumetric compression ranges from 40% to 80%, with the Poisson's ratio v_{21} ranging from −1 to 0 and tangent modulus E_{t2} from 0.2 MPa to 2 MPa. The auxetic foams obtained in this work possess good auxetic and stiffness properties compared to other open cell auxetic PU foams described in scientific literature

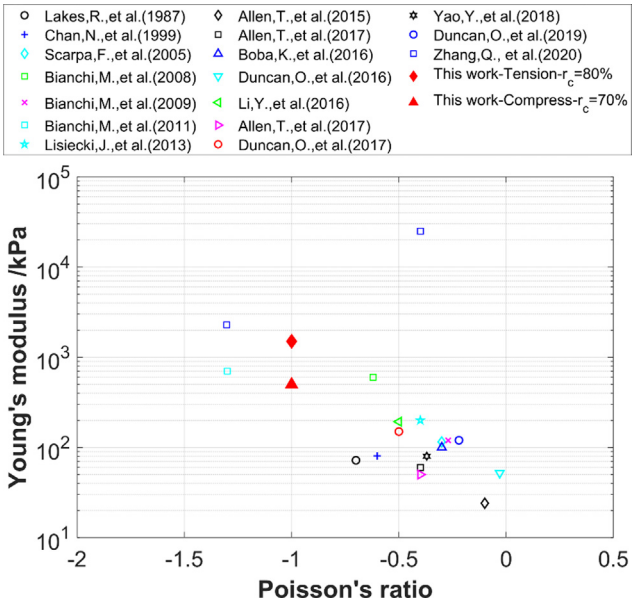

Fig. 16. Poisson's ratio and Young's modulus of open-cell auxetic PU foams in scientific literature. All moduli are calculated at small strains (within 20%).

[46] (Fig. 16). The stiffness of the foams described in this work is only lower than those previously made by the Authors using complex vacuum bag and autoclave. The topological characteristics of the auxetic foams have been extracted from a 3D model obtained by μ-CT scan. The scan shows that the auxetic foam has the majority of ribs with mean diameter of 0.03 mm, length of ~ 0.3 mm and the ribs oriented in transverse plane 2–3. The cell structures exhibit re-entrant shape along the thermoform compression direction 1. Finite Element models have been developed based on the μ-CT scanned 3D models and show a good agreement between the numerical and the experimental results. The FE results show that the inclined and curved re-entrant ribs inside the auxetic foam are stretched and straightened by tensile loading but twisted and bent under compression. The tensile modulus increases with the strain and is always larger than the compressive modulus (for strains < 10%). The auxeticity is caused by the deformation of the curved re-entrant cell structures. In this study we correlate the mechanical performance of auxetic foam by FE simulation based on real 3D structures from X-ray μ-CT scan, improving our understanding of the topological characteristics and internal deformation mechanisms occurring in auxetic porous materials.

Moreover, this work shows a simpler and cost-effective way to produce auxetic open cell polyurethane foam with large size, promoting the process of commercialization. The combination of high-resolution μ-CT techniques, three-dimensional skeletonization algorithms and FE simulation provides a persuasive analysis procedure for deformation mechanism and mechanical properties of porous materials not limited to foam materials.

CRediT authorship contribution statement

Qicheng Zhang: Conceptualization, Formal analysis, Investigation, Methodology, Validation, Software, Writing - original draft. **Wenjiang Lu:** Conceptualization, Investigation, Methodology, Formal analysis, Validation. **Fabrizio Scarpa:** Supervision, Validation, Funding acquisition, Project administration, Resources, Writing - final draft. **David Barton:** Supervision, Funding acquisition, Validation. **Kathryn Rankin:** Data curation, Software, Formal analysis. **Yunpeng Zhu:** Data curation, Validation. **Zi-Qiang Lang:** Project

administration, Resources. **Hua-Xin Peng:** Project administration, Resources.

Declaration of Competing Interest

The authors declare that they have no known competing financial interests or personal relationships that could have appeared to influence the work reported in this paper.

Acknowledgement

This project has been supported by the UK Engineering and Physical Sciences Research Council (EPSRC) EP/R032793/1 SYSDYMATS. FS and HXP acknowledge the support of the University of Bristol and Zhejiang University through the InCIS-ACCIS PhD Collaboration programme and ZJU's Overseas Academician Joint Lab for Advanced Composite Materials and Structures. The μ-CT scanning was conducted at the μ-VIS X-ray Imaging Centre, University of Southampton, supported by the National Research Facility for Lab X-ray CT (NXCT) through EPSRC grant EP/T02593X/1. HXP also acknowledges the support by the Fundamental Research Funds for the Central University.

Data availability statement

The raw/processed data required to reproduce these findings cannot be shared at this time due to technical or time limitations. Data will be shared in future in a repository available to open access.

References

[1] R. Critchley, I. Corni, J.A. Wharton, F.C. Walsh, R.J.K. Wood, K.R. Stokes, A review of the manufacture, mechanical properties and potential applications of auxetic foams, Phys. Stat. Sol. (b) (2013) 20.
[2] X. Ren, J. Shen, P. Tran, T.D. Ngo, Y.M. Xie, Design and characterisation of a tuneable 3D buckling-induced auxetic metamaterial, Mater. Des. 139 (2018) 336–342.
[3] N. Chan, K.E. Evans, Indentation Resilience of Conventional and Auxetic Foams, J. Cell. Plast. 34 (3) (1998) 231–260.
[4] N. Chan, K.E. Evans, The Mechanical Properties of Conventional and Auxetic Foams. Part II: Shear, J. Cell. Plast. 35 (2) (1999) 166–183.
[5] H.C. Cheng, F. Scarpa, T.H. Panzera, I. Farrow, H.-X. Peng, Shear Stiffness and Energy Absorption of Auxetic Open Cell Foams as Sandwich Cores, Phys. Stat. Sol. (b) 256 (1) (2019) 1800411, https://doi.org/10.1002/pssb:v256.110.1002/pssb:201800411.
[6] N. Novak, O. Duncan, T. Allen, A. Alderson, M. Vesenjak, Z. Ren, Shear modulus of conventional and auxetic open-cell foam, Mech. Mater. 157 (2021) 103818, https://doi.org/10.1016/j.mechmat.2021.103818.
[7] J.P. Donoghue, K.L. Alderson, K.E. Evans, The fracture toughness of composite laminates with a negative Poisson's ratio, Phys. Stat. Sol. (b) 246 (9) (2009) 2011–2017.
[8] R.S. Lakes, R. Witt, Making and Characterizing Negative Poisson's Ratio Materials, Int. J. Mech. Eng. Educ. 30 (1) (2002) 50–58.
[9] A. Alderson, K.L. Alderson, G. Chirima, N. Ravirala, K.M. Zied, The in-plane linear elastic constants and out-of-plane bending of 3-coordinated ligament and cylinder-ligament honeycombs, Compos. Sci. Technol. 70 (7) (2010) 1034–1041.
[10] S. Mohsenizadeh, R. Alipour, M. Shokri Rad, A. Farokhi Nejad, Z. Ahmad, Crashworthiness assessment of auxetic foam-filled tube under quasi-static axial loading, Mater. Des. 88 (2015) 258–268.
[11] M. Bianchi, F.L. Scarpa, C.W. Smith, Stiffness and energy dissipation in polyurethane auxetic foams, J. Mater. Sci. 43 (17) (2008) 5851–5860.
[12] S. Hou, T. Li, Z. Jia, L. Wang, Mechanical properties of sandwich composites with 3d-printed auxetic and non-auxetic lattice cores under low velocity impact, Mater. Des. 160 (2018) 1305–1321.
[13] S.N. Khaderi, N. Kumar, K.T. Rao, Impact on auxetic and metal foams, Vibroengineering PROCEDIA 29 (2019) 255–259.
[14] S. Hou, T. Liu, Z. Zhang, X.u. Han, Q. Li, How does negative Poisson's ratio of foam filler affect crashworthiness?, Mater Des. 82 (2015) 247–259.
[15] M. Bianchi, F. Scarpa, Vibration transmissibility and damping behaviour for auxetic and conventional foams under linear and nonlinear regimes, Smart Mater. Struct. 22 (8) (2013) 084010, https://doi.org/10.1088/0964-1726/22/8/084010.
[16] M. Bianchi, F. Scarpa, C.W. Smith, Shape memory behaviour in auxetic foams: Mechanical properties, Acta Mater. 58 (3) (2010) 858–865.
[17] M. Bianchi, F. Scarpa, C.W. Smith, G.R. Whittell, Physical and thermal effects on the shape memory behaviour of auxetic open cell foams, J. Mater. Sci. 45 (2) (2010) 341–347.
[18] D. Fan, Z. Shi, N. Li, J. Qiu, H. Xing, Z. Jiang, M. Li, T. Tang, Novel Method for Preparing a High-Performance Auxetic Foam Directly from Polymer Resin by a One-Pot CO2 Foaming Process, ACS Appl. Mater. Interfaces 12 (42) (2020) 48040–48048.
[19] D. Fan, M. Li, J. Qiu, H. Xing, Z. Jiang, T. Tang, Novel Method for Preparing Auxetic Foam from Closed-Cell Polymer Foam Based on the Steam Penetration and Condensation Process, ACS Appl. Mater. Interfaces 10 (26) (2018) 22669–22677.
[20] R. Gatt, D. Attard, E. Manicaro, E. Chetcuti, J.N. Grima, On the effect of heat and solvent exposure on the microstructure properties of auxetic foams: A preliminary study, Phys. Stat. Sol. (b) 248 (1) (2011) 39–44.
[21] Y. Yao, Y. Luo, Y. Xu, B. Wang, J. Li, H. Deng, H. Lu, Fabrication and characterization of auxetic shape memory composite foams, Compos. B Eng. 152 (2018) 1–7.
[22] T. Allen, J. Shepherd, T.A.M. Hewage, T. Senior, L. Foster, A. Alderson, Low-kinetic energy impact response of auxetic and conventional open-cell polyurethane foams, Phys. Stat. Sol. (b) 252 (7) (2015) 1631–1639.
[23] T. Allen, N. Martinello, D. Zampieri, T. Hewage, T. Senior, L. Foster, A. Alderson, Auxetic Foams for Sport Safety Applications, Procedia Eng. 112 (2015) 104–109.
[24] F. Scarpa, J. Giacomin, Y. Zhang, P. Pastorino, Mechanical Performance of Auxetic Polyurethane Foam for Antivibration Glove Applications, Cell. Polym. 24 (5) (2005) 253–268.
[25] H. Mohanraj, S.L.M. Filho Ribeiro, T.H. Panzera, F. Scarpa, I.R. Farrow, R. Jones, A. Davies-Smith, C.D.L. Remillat, P. Walters, H.-X. Peng, Hybrid auxetic foam and perforated plate composites for human body support, Phys. Stat. Sol. (b) 253 (7) (2016) 1378–1386.
[26] F. Scarpa, F.C. Smith, Passive and MR Fluid-coated Auxetic PU Foam – Mechanical, Acoustic, and Electromagnetic Properties, J. Intell. Mater. Syst. Struct. 15 (12) (2004) 973–979.
[27] B. Howell, P. Prendergast, L. Hansen, Examination of acoustic behavior of negative poisson's ratio materials, Appl. Acoust. 43 (2) (1994) 141–148.
[28] J.-H. Oh, J.-S. Kim, V.H. Nguyen, I.-K. Oh, Auxetic graphene oxide-porous foam for acoustic wave and shock energy dissipation, Compos. B Eng. 186 (2020) 107817, https://doi.org/10.1016/j.compositesb:2020.107817.
[29] Y.-C. Wang, R. Lakes, Analytical parametric analysis of the contact problem of human buttocks and negative Poisson's ratio foam cushions, Int. J. Solids Struct. 39 (18) (2002) 4825–4838.
[30] M. Janus-Michalska, D. Jasińska, J. Smardzewski, Comparison of Contact Stress Distribution for Foam Seat and Seat of Auxetic Spring Skeleton, Int. J. Appl. Mech. Eng. 18 (1) (2013) 55–72.
[31] A. Alderson, J. Rasburn, K.E. Evans, J.N. Grima, Auxetic polymeric filters display enhanced de-fouling and pressure compensation properties, Membr. Technol. 2001 (137) (2001) 6–8.
[32] A. Alderson, J. Rasburn, K.E. Evans, Mass transport properties of auxetic (negative Poisson's ratio) foams, Phys. Stat. Sol. (b) 244 (3) (2007) 817–827.
[33] A. Alderson, K.L. Alderson, S.A. McDonald, B. Mottershead, S. Nazare, P.J. Withers, Y.T. Yao, Piezomorphic Materials, Macromol. Mater. Eng. 298 (3) (2013) 318–327.
[34] S.L. Zhang, Y.-C. Lai, X.u. He, R. Liu, Y. Zi, Z.L. Wang, Auxetic Foam-Based Contact-Mode Triboelectric Nanogenerator with Highly Sensitive Self-Powered Strain Sensing Capabilities to Monitor Human Body Movement, Adv. Funct. Mater. 27 (25) (2017) 1606695, https://doi.org/10.1002/adfm.v27.2510.1002/adfm.201606695.
[35] M.F. Ahmed, Y. Li, C. Zeng, Stretchable and compressible piezoresistive sensors from auxetic foam and silver nanowire, Mater. Chem. Phys. 229 (2019) 167–173.
[36] F. La Malfa, S. Puce, F. Rizzi, M. De Vittorio, A Flexible Carbon Nanotubes-Based Auxetic Sponge Electrode for Strain Sensors, Nanomaterials (Basel) 10 (12) (2020).
[37] R. Lakes, Foam structures with a negative poissons ratio, Science 235 (4792) (1987) 1038–1040.
[38] M. Bianchi, F. Scarpa, M. Banse, C.W. Smith, Novel generation of auxetic open cell foams for curved and arbitrary shapes, Acta Mater. 59 (2) (2011) 686–691.
[39] N. Chan, K.E. Evans, Fabrication methods for auxetic foams, J. Mater. Sci. 32 (22) (1997) 5945–5953.
[40] O. Duncan, T. Allen, L. Foster, T. Senior, A. Alderson, Fabrication, characterisation and modelling of uniform and gradient auxetic foam sheets, Acta Mater. 126 (2017) 426–437.
[41] Saeid Mohsenizadeh, Zaini Ahmad, Roozbeh Alipour, Rohah A. Majid, Yunan Prawoto, Quasi Tri-Axial Method for the Fabrication of Optimized Polyurethane Auxetic Foams, Phys. Stat. Sol. (b) 256 (10) (2019) 1800587, https://doi.org/10.1002/pssb:v256.1010.1002/pssb:201800587.
[42] F Pierron, Identification of Poisson's ratios of standard and auxetic low-density polymeric foams from full-field measurements, J. Strain Anal. Eng. Des. 45 (4) (2010) 233–253.
[43] Yan Li, Changchun Zeng, Room-Temperature, Near-Instantaneous Fabrication of Auxetic Materials with Constant Poisson's Ratio over Large Deformation, Adv Mater 28 (14) (2016) 2822–2826.
[44] Joseph N. Grima, Daphne Attard, Ruben Gatt, Richard N. Cassar, A Novel Process for the Manufacture of Auxetic Foams and for Their re-Conversion to Conventional Form, Adv. Eng. Mater. 11 (7) (2009) 533–535.

[45] F. Scarpa, P. Pastorino, A. Garelli, S. Patsias, M. Ruzzene, Auxetic compliant flexible PU foams: static and dynamic properties, Phys. Stat. Sol. (b) 242 (2005) 681–694.
[46] Qicheng Zhang, Wenjiang Lu, Fabrizio Scarpa, David Barton, Roderic S. Lakes, Yunpeng Zhu, Ziqiang Lang, Hua-Xin Peng, Large stiffness thermoformed open cell foams with auxeticity, Appl. Mater. Today 20 (2020) 100775, https://doi.org/10.1016/j.apmt.2020.100775.
[47] Kim Alderson, Andrew Alderson, Naveen Ravirala, Virginia Simkins, Philip Davies, Manufacture and characterisation of thin flat and curved auxetic foam sheets, Phys. Stat. Sol. (b) 249 (7) (2012) 1315–1321.
[48] N. Chan, K.E. Evans, Microscopic examination of the microstructure and deformation of conventional and auxetic foams, J. Mater. Sci. 32 (21) (1997) 5725–5736.
[49] A. Bezazi, F. Scarpa, Mechanical behaviour of conventional and negative Poisson's ratio thermoplastic polyurethane foams under compressive cyclic loading, Int. J. Fatigue 29 (5) (2007) 922–930.
[50] Samuel A. McDonald, Ghislain Dedreuil-Monet, Yong Tao Yao, Andrew Alderson, Philip J. Withers, In situ 3D X-ray microtomography study comparing auxetic and non-auxetic polymeric foams under tension, Phys. Stat. Sol. (b) 248 (1) (2011) 45–51.
[51] F. Pierron, S.A. McDonald, D. Hollis, J. Fu, P.J. Withers, A. Alderson, Comparison of the Mechanical Behaviour of Standard and Auxetic Foams by X-ray Computed Tomography and Digital Volume Correlation, Strain 49 (6) (2013) 467–482.
[52] J. Lisiecki, S. Kłysz, T. Błażejewicz, G. Gmurczyk, P. Reymer, Tomographic examination of auxetic polyurethane foam structures, Phys. Stat. Sol. (b) 251 (2) (2014) 314–320.
[53] Katarzyna Boba, Matteo Bianchi, Greg McCombe, Ruben Gatt, Anselm C. Griffin, Robert M. Richardson, Fabrizio Scarpa, Ian Hamerton, Joseph N. Grima, Blocked Shape Memory Effect in Negative Poisson's Ratio Polymer Metamaterials, ACS Appl. Mater. Interfaces 8 (31) (2016) 20319–20328.
[54] O. Duncan, F. Clegg, A. Essa, A.M.T. Bell, L. Foster, T. Allen, A. Alderson, Effects of Heat Exposure and Volumetric Compression on Poisson's Ratios, Young's Moduli, and Polymeric Composition During Thermo-Mechanical Conversion of Auxetic Open Cell Polyurethane Foam, Phys. Stat. Sol. (b) 256 (1) (2019).
[55] Wen-Yea Jang, Andrew M. Kraynik, Stelios Kyriakides, On the microstructure of open-cell foams and its effect on elastic properties, Int. J. Solids Struct. 45 (7-8) (2008) 1845–1875.
[56] A. Jung, J. Luksch, S. Diebels, F. Schäfer, C. Motz, In-situ and ex-situ microtensile testing of individual struts of Al foams and Ni/Al hybrid foams, Mater. Des. 153 (2018) 104–119.
[57] T.F. Zhao, Z.C. Deng, C.Y. Fu, X.J. Wang, H.Y. Zhou, C.Q. Chen, Thickness effect on mechanical behavior of auxetic sintered metal fiber sheets, Mater. Des. 167 (2019) 107635, https://doi.org/10.1016/j.matdes.2019.107635.
[58] Yanhong Ma, Qicheng Zhang, Yongfeng Wang, Jie Hong, Fabrizio Scarpa, Topology and mechanics of metal rubber via X-ray tomography, Mater. Des. 181 (2019) 108067, https://doi.org/10.1016/j.matdes.2019.108067.
[59] X. Huang, Q. Wang, W. Zhou, J. Li, A simple fracture energy prediction method for fiber network based on its morphological features extracted by X-ray tomography, Mater. Sci. Eng., A 585 (2013) 297–303.
[60] Qinghui Wang, Xiang Huang, Wei Zhou, Jingrong Li, Three-dimensional reconstruction and morphologic characteristics of porous metal fiber sintered sheet, Mater. Charact. 86 (2013) 49–58.
[61] J.V. Emmanuel Brun, Frédéric Topin, René Occelli, Geometrical measurement of real foams from 3d images, Metfoam 2007, Montreal, 2007.
[62] J. Vicente, F. Topin, J.V. Daurelle, Open Celled Material Structural Properties Measurement: From Morphology to Transport Properties, Mater. Trans. 47 (9) (2006) 2195–2202.
[63] J.A. Elliott, A.H. Windle, J.R. Hobdell, G. Eeckhaut, R.J. Oldman, W. Ludwig, E. Boller, P. Cloetens, J. Baruchel, In-situ deformation of an open-cell flexible polyurethane foam characterised by 3D computed microtomography, J. Mater. Sci. 37 (8) (2002) 1547–1555.
[64] N. Gaspar, C.W. Smith, E.A. Miller, G.T. Seidler, K.E. Evans, Quantitative analysis of the microscale of auxetic foams, Phys. Stat. Sol. (b) 242 (3) (2005) 550–560.
[65] W.E. Warren, A.M. Kraynik, Linear Elastic Behavior of a Low-Density Kelvin Foam With Open Cells, J. Appl. Mech. 64 (4) (1997) 787–794.
[66] J.B. Choi, R.S. Lakes, Analysis of elastic modulus of conventional foams and of re-entrant foam materials with a negative Poisson's ratio, Int. J. Mech. Sci. 37 (1) (1995) 51–59.
[67] J.B. Choi, R.S. Lakes, Nonlinear Analysis of the Poisson's Ratio of Negative Poisson's Ratio Foams, J. Compos. Mater. 29 (1) (1995) 113–128.
[68] E. Chetcuti, B. Ellul, E. Manicaro, J.-P. Brincat, D. Attard, R. Gatt, J.N. Grima, Modeling auxetic foams through semi-rigid rotating triangles, Phys. Stat. Sol. (b) 251 (2) (2014) 297–306.
[69] J. Fu, H.R. Thomas, C. Li, Tortuosity of porous media: Image analysis and physical simulation, Earth Sci. Rev. 212 (2021).
[70] C. Defonseka, Practical Guide to Flexible Polyurethane Foams, Smithers Information Limited, 2013.
[71] N. Chan, K.E. Evans, The Mechanical Properties of Conventional and Auxetic Foams. Part I: Compression and Tension, J. Cell. Plast. 35 (2) (1999) 130–165.
[72] H.J. Qi, M.C. Boyce, Stress–strain behavior of thermoplastic polyurethanes, Mech. Mater. 37 (8) (2005) 817–839.
[73] S.S. Sarva, S. Deschanel, M.C. Boyce, W. Chen, Stress–strain behavior of a polyurea and a polyurethane from low to high strain rates, Polymer 48 (8) (2007) 2208–2213.
[74] G. Batt, Primary Resonance Behavior of Expanded Polymer Cushion Material Under Low-Intensity Harmonic Excitations, Clemson University, 2013.
[75] R.W. Ogden, D.G. Roxburgh, A pseudo–elastic model for the Mullins effect in filled rubber, Proc. Roy. Soc. Lond. Series A: Math. Phys. Eng. Sci. 455 (1988) (1999) 2861–2877.
[76] D. Zhang, F. Scarpa, Y. Ma, K. Boba, J. Hong, H. Lu, Compression mechanics of nickel-based superalloy metal rubber, Mater. Sci. Eng., A 580 (2013) 305–312.
[77] S.R. Reichhold, Effective elastic constants of fiber-reinforced polymer-matrix composites with the concept of interphase, 2002.
[78] C.T. Sun, R.S. Vaidya, Prediction of composite properties from a representative volume element, Compos. Sci. Technol. 56 (2) (1996) 171–179.
[79] H.M.C.C. Somarathna, S.N. Raman, D. Mohotti, A.A. Mutalib, K.H. Badri, Hyper-viscoelastic constitutive models for predicting the material behavior of polyurethane under varying strain rates and uniaxial tensile loading, Constr. Build. Mater. 236 (2020).
[80] W. Lu, F. Qin, Y. Wang, Y. Luo, H. Wang, F. Scarpa, J. Li, R. Sesana, F. Cura, H.X. Peng, Engineering Graphene Wrinkles for Large Enhancement of Interlaminar Friction Enabled Damping Capability, ACS Appl. Mater. Interfaces 11 (33) (2019) 30278–30289.